REVIEW

Heterometallic nanomaterials: activity modulation, sensing, imaging and therapy

Shan-Shan Li,[a] Ai-Jun Wang, [ID] [b] Pei-Xin Yuan, [ID] [b] Li-Ping Mei, [ID] [b] Lu Zhang [ID] [b] and Jiu-Ju Feng [ID] *[b]

Heterometallic nanomaterials (HMNMs) display superior physicochemical properties and stability to monometallic counterparts, accompanied by wider applications in the fields of catalysis, sensing, imaging, and therapy due to synergistic effects between multi-metals in HMNMs. So far, most reviews have mainly concentrated on introduction of their preparation approaches, morphology control and applications in catalysis, assay of heavy metal ions, and antimicrobial activity. Therefore, it is very important to summarize the latest investigations of activity modulation of HMNMs and their recent applications in sensing, imaging and therapy. Taking the above into consideration, we briefly underline appealing chemical/physical properties of HMNMs chiefly tailored through the sizes, shapes, compositions, structures and surface modification. Then, we particularly emphasize their widespread applications in sensing of targets (*e.g.* metal ions, small molecules, proteins, nucleic acids, and cancer cells), imaging (frequently involving photoluminescence, fluorescence, Raman, electrochemiluminescence, magnetic resonance, X-ray computed tomography, photoacoustic imaging, *etc.*), and therapy (*e.g.* radiotherapy, chemotherapy, photothermal therapy, photodynamic therapy, and chemodynamic therapy). Finally, we present an outlook on their forthcoming directions. This timely review would be of great significance for attracting researchers from different disciplines in developing novel HMNMs.

1. Introduction

In recent years, monometallic nanomaterials (MMNMs) have found widespread applications in optics, catalysis, energy and life sciences, thanks to their intrinsic advantages (*e.g.* good stability and biocompatibility, high catalytic properties, and superior electronic conductivity) over bulk counterparts.[1–4] As demonstrated by previous studies, their unique chemical and physical properties (*e.g.* chemical stability, and electrical and optical properties) mainly originate from tunneling effect, quantum size effect, and surface effect. Such properties can be finely modulated by controlling the size, composition, morphology, architecture, surface functionalization, and crystal structure/phase.[4,5]

To achieve their scalable design and synthesis, a series of synthesis methods have been developed, including electrode-position, wet-chemical synthesis, hydrothermal treatment, and sonochemical methods.[4–7] Accordingly, diverse micro-/nano-structures have been constructed (*e.g.* sheets, wires, dendrites, tubes and particles), showing wide applications in the aforementioned fields,[1,4,7] in spite of their limited resources and high price, along with instability. For their potential application, it is ideal yet challenging to simultaneously combine low cost, superior optical/electrical properties, and good stability, although this point is difficult to satisfy only with MMNMs.

To meet the requirements, substantial efforts have been made towards synthesis of advanced heterometallic nano-materials (HMNMs) in the past several decades. Generally, doping with a second or even third metal can greatly change spatial arrangement patterns, local bonding geometry (structural effects), and distributions of active sites (ensemble effects) to enable easy availability of more active sites, coupled with revival of activity of surface atoms (electronic effects), which in turn improves the physicochemical properties,[8,9] owing to synergistic impacts of multiple metals in HMNMs.[10,11] As a result, HMNMs have wider applications than MMNMs in the fields of sensing, imaging and therapy.

For preparation of HMNMs, reduction of metal precursors and disassembly of a larger object are two common routes, termed as bottom-up and top-down methods, respectively.[7,12] The former requires suitable metal salts, reducing agent(s) and solvents. Notably, some solvents such as polyols and amines can simultaneously work as reducing agents.[13–15] Also, some surfactants, polymers and polyelectrolytes are usually required for metal crystal growth and colloidal stability, coupled with

[a]Institute for Chemical Biology & Biosensing, College of Life Sciences, Qingdao University, 308 Ningxia Road, Qingdao, 266071, China

[b]Key Laboratory of the Ministry of Education for Advanced Catalysis Materials, College of Chemistry and Life Sciences, College of Geography and Environmental Sciences, Zhejiang Normal University, Jinhua 321004, China. E-mail: jjfeng@zjnu.cn

Fig. 1 Overview of the activity modulation of HMNMs and their diverse applications.

regulation of synthesis parameters (*i.e.* reaction temperature, reaction time, reagent concentration, *etc.*). In short, the bottom-up approach commonly involves co-reduction, seeded-growth, and anodic dissolution.[7,12] Alternatively, the top-down method is an effective way to prepare HMNMs, although it is less used than the bottom-up counterpart.[12] Particularly, laser ablation is a highly controllable top-down method, where well-dispersed HMNMs are harvested upon applying a laser beam on a solid target.[16]

Up to date, early reviews have mainly focused on introducing preparation methods, morphology control, and applications of metal nanomaterials in catalysis,[1,2,7] determination of heavy metal ions[17] and antimicrobial activity.[18] Nevertheless, most of the outlined applications correlate to MMNMs,[17,18] while scarcely involving HMNMs. To this end, this review mainly introduces the latest developments in activity modulation of HMNMs by finely regulating the shape, size, composition, configuration and surface modification, coupled with outlining their main applications in sensing, imaging and therapy within past five years due to the article length limitation (Fig. 1). Finally, an outlook on their forthcoming directions is provided. This timely review would be instructive to deeply illustrate the correlations between the physicochemical properties and synthetic parameters of HMNMs, and provide some valuable insights for researchers from different disciplines (*e.g.* chemistry, materials science, biology and nanotechnology).

2. Tailoring the physicochemical properties of HMNMs

To our knowledge, the chemical and physical properties of HMNMs as well as their advanced applications correlate with their architecture, surface atomic arrangement, and coordination. The properties have close correlation with their size, morphology, and compositions.[19–21] Lin *et al.* constructed bimetallic Au–Bi nanoparticles (NPs) with a size of about 5 nm, which exhibited a significantly improved thermal effect under the same light radiation.[19] Hou and co-workers prepared Au_3Cu

tetrapod nanocrystals (TPNCs) for multi-modal image-guided photothermal therapy (PTT) within the second near-infrared (NIR-II) region.[20] In addition to size and morphology, we also investigated the influences of compositions, structures, and surface modification on the properties of HMNMs and the hybrid composites.

2.1 Sizes

Size of HMNMs is crucial to their properties, due to the well-known size effect.[9,19,21] Plainly, reducing their size can greatly improve their utilization with the purpose to increase the occupancy ratio of surface atoms, ultimately improving their physical/chemical properties.[22] For instance, Quan's group synthesized ultra-small FePd nanodots (around 3.4 nm), exhibiting good photothermal conversion efficiency (PCE) in the NIR-II region.[9] In another case, a trimetallic (triM) PdCuFe alloy was prepared with a diameter of 5.5 nm, which worked as a stimulus to activate Fenton reactors for chemodynamic therapy (CDT).[21] In addition, the size of the nanodots can be finely tailored using different precursor types and other synthesis conditions (*i.e.* reaction temperature, reaction speed, duration, *etc.*).[23] The resultant nanodots exhibited good biocompatibility, and can be easily removed because of their small size.

Besides, Au–Ag bimetallic nanoclusters (BNCs) displaying efficient NIR-II aqueous electrochemiluminescence (ECL) were synthesized by combining Au nanoclusters with Ag, which were applied for selective analysis of a carbohydrate antigen (CA125).[24] Jia and co-workers reported ultra-small bovine serum albumin-directed Au–Ag (Au–Ag@BSA) NPs with a size range of 2–4 nm, which showed great promise as a contrast agent in X-ray computed tomography (CT).[25]

2.2 Morphology

For HMNMs, their physicochemical properties not only are related to the particle sizes, but also closely depend on their shapes.[26–28] Among them, there appear many Au/Pt-based nanostructures with a variety of shapes (*e.g.* particles, sheets, dendrites, flowers, multipods and stars) used in analysis, imaging and therapy (Fig. 2), mainly attributing to their good biocompatibility, high stability, easy modification, excellent catalytic properties, and tunable plasmon properties.[20,26,27,29–34]

Recently, dendrite-like architectures of HMNMs have attracted substantial attention because of their appealing properties, owing to more steps, edges and corners that would create more active sites facilely available.[26,35,36] For example, Pan and co-workers developed PEGylated Au@Pt nanodendrites as an enhanced theranostic agent for CT imaging and photothermal/radiation therapy (Fig. 2C).[26] Clearly, the absorption of Au@Pt nanodendrites positively shifts to the NIR region upon gradual growth of Pt nanobranches, thereby enhancing efficacy of PTT and radiation therapy within cancer cells.

Meanwhile, core/shell structures usually have specific core/shell configurations, and attract tremendous interest owing to their magnified surface area and low density. Jokerst's group
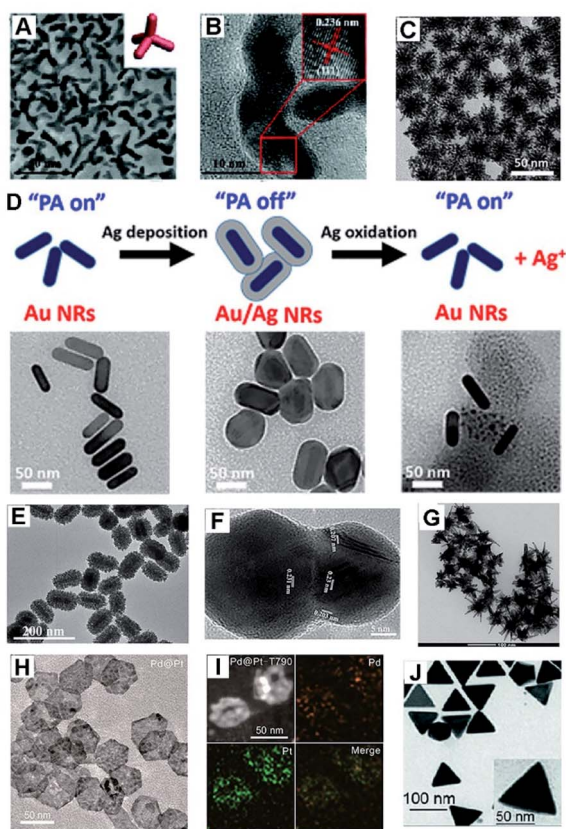
Fig. 2 (A) TEM image of Au₃Cu TPNCs. Inset shows the geometric model. (B) HR–TEM image of Au₃Cu TPNCs. Reproduced with permission.[20] Copyright 2018, The Royal Society of Chemistry. (C) TEM image of Au@Pt nanodendrites. Reproduced with permission.[26] Copyright 2017, American Chemical Society. (D) Schematic diagram of the experiment and TEM images of Au NRs, Au/Ag NRs, and etched Au/Ag NRs. Reproduced with permission.[27] Copyright 2018, American Chemical Society. (E) TEM images of mulberry-like Au@PtPd porous nanorods. Reproduced with permission.[30] Copyright 2020, Elsevier. (F) HR–TEM image of a Au/Ag alloy nanopeanut. Reproduced with permission.[31] Copyright 2019, Elsevier. (G) TEM image of Au/Pt stars. Reproduced with permission.[32] Copyright 2020, Springer. (H) TEM image of Pd@Pt nanoplates. (I) HAADF–STEM image and elemental mapping of Pd@Pt–T790. Reproduced with permission.[33] Copyright 2020, American Chemical Society. (J) TEM image of the Au@Ag triangular NPs. Reproduced with permission.[34] Copyright 2018, The Royal Society of Chemistry.

developed Au nanorods with a Ag shell (Au/Ag NRs), and the Ag shell can be further etched away with ferricyanide, ultimately achieving photoacoustic (PA) imaging and a good antibacterial effect (Fig. 2D).[27]

Hierarchical porous nanostructures have large specific surface areas and low density, which offer more active sites due to rich atomic steps, edges and corner atoms on the interconnected structures compared to solid counterparts.[37–39] Besides, such unique configurations can efficiently suppress Ostwald ripening effects, consequently improving operation stability. Lately, porous Au@Pt NPs were physically absorbed with doxorubicin (DOX) and then chemically conjugated with cRGD (a cell penetrating peptide), which displayed strong NIR

absorbance and high photo-conversion efficiency for PA image-guided enhanced PTT of MDA-MB-231 tumors.[29] Similarly, mulberry-like Au@PtPd porous nanorods were prepared, which worked as signal amplifiers for sensitive detection of carcinoembryonic antigen (CEA) with satisfactory results even in human serum samples (Fig. 2E).[30]

Also, porous Au@Rh nanostructures displayed catalase-like activity, and was further coated with tumor cell membrane (CM) and photosensitizer indocyanine green (ICG). As a result, *in vitro* and *in vivo* observations of the Au@Rh-ICG-CM certify effective transformation of endogenous hydrogen peroxide (H_2O_2) to oxygen and a boost in production of tumor-toxic singlet oxygen, thereby significantly enhancing oxygen-dependent cancer photodynamic therapy (PDT).[28]

Aside from the above, Au-, Pt-, and/or Pd-based nanoplates or nanotriangles demonstrate intense NIR absorption and large specific surface area, showing extensive applications in anti-bacterial and therapy fields.[33,34,40,41] For example, Pd@Pt nanoplates were successfully bridged with *meso*-tetra(4-carboxyphenyl)porphine (T790) for catalysis-enhanced ultrasound (US)-driven sonodynamic therapy (SDT) to treat methicillin-resistant *Staphylococcus aureus* (MRSA)-infected myositis (Fig. 2H and I).[33] Notably, T790 anchored on Pd@Pt can effectively inhibit the catalase-like activity, while their enzyme-like activity was recovered under irradiation by catalytic decomposition of endogenous H_2O_2 to O_2 in bacterial infections. A similar observation was found when using two-dimensional (2D) Pd@Au core–shell nanostructures with the purpose to alleviate tumor hypoxia, which in turn significantly improved the cancer radiotherapy (RT) outcomes.[40]

2.3 Compositions

In general, HMNMs receive greater interest than MMNMs from both technological and scientific perspectives, and display superior physiochemical properties and stability to monometallic counterparts.[1,7,42,43] Their improved physical and chemical performances mainly stem from geometric (ensemble effect), electronic (ligand effect), and synergistic effects associated with different metals as reported in the literature.[21,44,45] As earlier certified, doping noble metal(s) with nonprecious transition metal(s) (M = Fe, Co, Cu, Ni, *etc.*) is feasible for constructing advanced HMNMs with desired compositions, particularly accompanied by less usage of noble metal(s), improved physicochemical properties and operation durability.[9,21,46,47] For example, ultra-small cysteine (Cys)-functionalized FePd nanodots were synthesized, which exhibited highly effective hyperthermia upon irradiation in the NIR-II region, and eventually showed a largely enhanced radiation effect for triple-modal imaging and thermo-RT.[9]

It is known that Pd is commonly recognized as a photothermal agent with high efficiency, having great potential in PTT.[48] Besides, Fe is an important element in human body for its magnetism, and often behaves as a contrast agent for magnetic resonance (MR) scanning.[23] Recently, an ultra-small PdCuFe alloy nanozyme was prepared, which showed cascade glutathione peroxidase (GSH-Px) and peroxidase (POD)

mimicking activities in circumneutral pH with a high PCE (62%) for synergistic tumor cell apoptosis, coupled with US-promoted tumor-specific CDT in the NIR window, exemplifying a multi-functional nanoenzyme design towards tumor inhibition.[21] In addition, the incorporated Fe well retained catalytic activity of Pd and displayed a lower cost to some extent.

Also, porous PdPtCoNi@Pt-skin nanopolyhedra were fabricated in our laboratory to build a sandwich-like electrochemical sensor for ultrasensitive assay of creatine kinase-MB (CK-MB).[46] Similarly, PtCoCuPd hierarchical branch-like tripods were constructed to develop an immunosensor for bioanalysis of cardiac troponin I (cTnI).[47] These examples demonstrate that the optimized compositions in HMNMs provide a widespread prospect in establishment of ultra-sensitive electrochemical immunosensors.[46,47,49–52]

Interestingly, metallic Janus nanoparticles (JNPs) represent effective combination of two or even more chemically discrepant metals into one single system.[53,54] They attract tremendous interest as they integrate multi-functional properties, and simultaneously perform more synergistic functions particularly in analytical chemistry.[55–58] Lately, Au–Pt JNPs were fabricated and their catalytic oxidation of a luminophore was examined by ECL microscopy, where single Au and Pt counterparts acted as references.[55] As seen from elemental mapping images, Au–Pt JNPs exhibited asymmetrical structures formed with equivalent Au and Pt (Fig. 3A), and showed distinctly boosted ECL intensity and stability, manifesting a superior catalytic effect compared to individual Au and Pt NPs.

Similarly, monodisperse Au–Fe$_2$C JNPs were prepared *via* a three-step strategy: Au seeds, Au–Fe heterostructures, and Au–Fe$_2$C JNPs (Fig. 3B–F).[56] The resulting Au–Fe$_2$C JNPs exhibited significant PCE and prominent magnetic properties, thanks to the associated absorption peak located in the NIR window coupled with incorporated Fe as an essential composition. As well, Au–Ag JNPs were prepared with stable and enhanced SERS activity (Fig. 3G), and further explored for building a ratiometric surface enhanced Raman scattering (SERS) sensor for quantitative assay of ochratoxin A (OTA).[57] What's more, a hollow Janus hybrid nanozyme was designed by bifacial regulation of Ag–Au nanocages (Fig. 3H and I), which effectively worked as a SERS liquid biopsy platform for determination of tumor-related biomarkers.[58] These successful examples certify the critical roles of compositions in fine modulation of the activity.

2.4 Structures

As we know, noble metal-based nanostructures have attracted significant attention in drug delivery, therapeutics and biosensing fields; however, their high cost is a main problem.[17,18,59] To circumvent this, it is attractive to employ HMNMs rather than MMNMs. In general, HMNMs mainly contain alloyed, porous and hollow structures. Plainly, alloyed HMNMs show interesting chemical and physical properties by virtue of the synergistic effect derived from incorporated metals, outperforming individual ones.[7] Alternatively, porous structures frequently have larger specific surface areas and create more active sites due to the abundant atomic steps, edges and corner
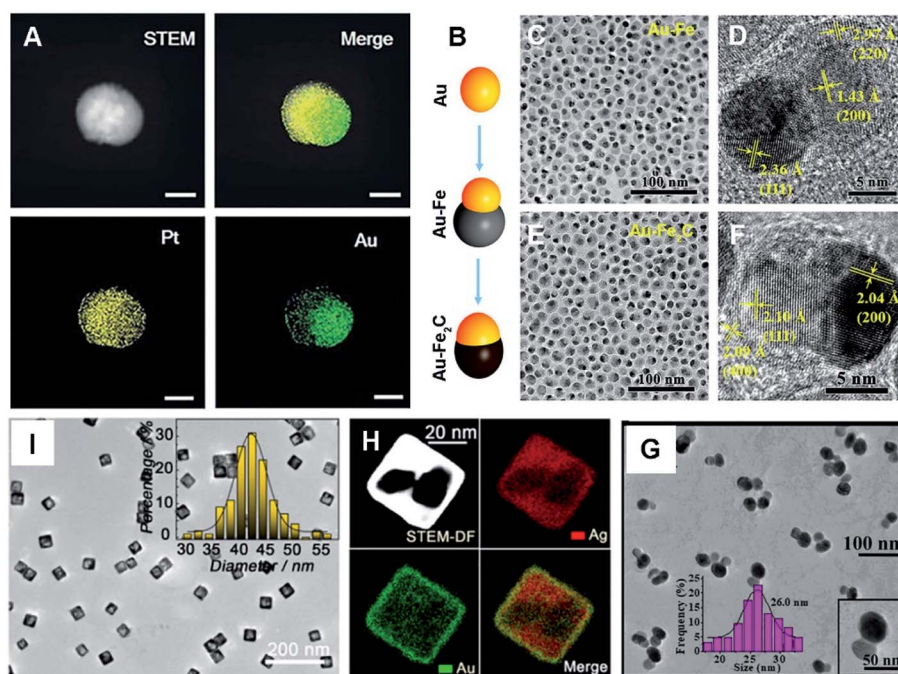

Fig. 3 (A) HAADF-STEM image and elemental mapping of a Au−Pt JNP, scale bar: 25 nm. Reproduced with permission.[55] Copyright 2018, Wiley. (B) Schematic diagram of the synthesis process of Au−Fe$_2$C JNPs. TEM images of Au−Fe heterostructures (C and D) and Au−Fe$_2$C JNPs (E and F). Reproduced with permission.[56] Copyright 2017, American Chemical Society. (G) TEM image of Au−Ag$_{(3)}$ JNPs and the corresponding size distribution. Reproduced with permission.[57] Copyright 2019, American Chemical Society. (I) TEM image of Ag−Au nanocages. The inset shows the size distribution. (H) HAADF-STEM image and elemental mapping of Ag−Au nanocages. Reproduced with permission.[58] Copyright 2019, American Chemical Society.
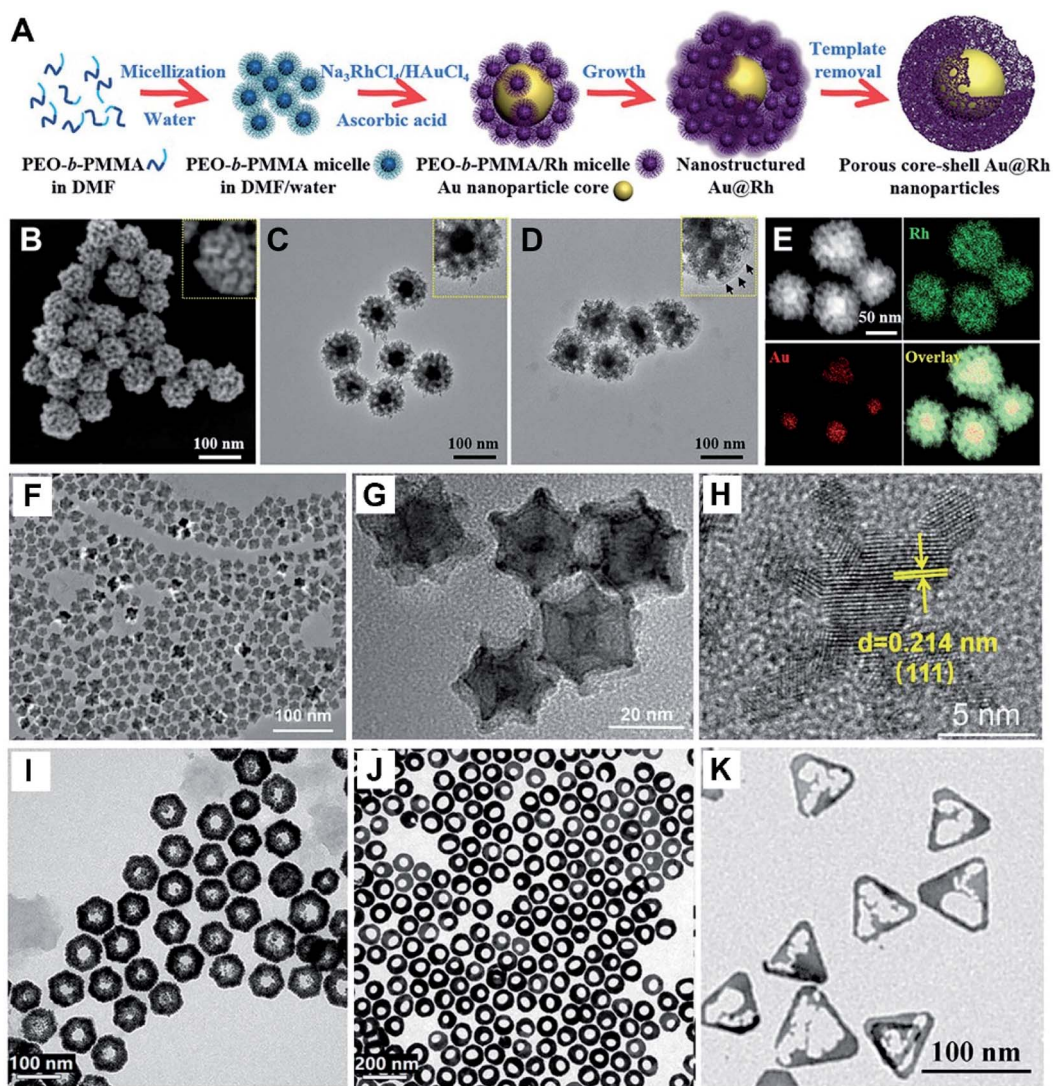
Fig. 4 (A) Schematic diagram of the preparation process of porous Au@Rh nanomaterials. (B) SEM image of Au@Rh nanomaterials. (C) TEM image of Au@Rh nanomaterials. (D) TEM image of Au@Rh-CM nanomaterials. (E) HAADF-STEM image and elemental mapping of Au and Rh. Reproduced with permission.[28] Copyright 2020, Wiley. TEM (F and G) and HR-TEM (H) images of PtCu$_3$ nanocages. Reproduced with permission.[63] Copyright 2019, Wiley. TEM images of Au@Pt nanodisks (I) and Pt@Au nanorings (J). Reproduced with permission.[66] Copyright 2019, American Chemical Society. (K) TEM image of Au–Ag HTNs. Reproduced with permission.[67] Copyright 2020, Springer.

atoms on such interconnected structures, accompanied by effective suppression of Ostwald ripening effects, consequently showing scalable optical/electrochemical properties and improved durability in contrast with solid counterparts.[28,29,37,60]

For instance, porous Au@Rh nanostructures were fabricated as a therapeutic reagent upon loading the pores with a photosensitizer, combined with parcelling with CM (Fig. 4A–E).[28] The nanocomposite improved the loading and simultaneously stabilized the activity of the photosensitizer during the biotransportation process without any premature release. The unique core–shell structure and porous shell confirmed ready availability of the two metals exposed to the reactants, modulating the core/shell boundary interactions via electronic and surface strain effects, in turn achieving the best catalytic performance.[61] Additionally, the porous structure can effectively

trap therapeutic drugs.[62] Other representative examples include porous Au@Pt NPs for relieving oxidative stress damage (OSD) and chemo-photothermal co-therapy,[29] as well as porous Au–Ag nanorods with sufficient internal hotspots for highly sensitive SERS detection.[60]

Three-dimensional (3D) hollow architectures have highly open structures and molecular surfaces with high density of active sites, which increase the loading capacity of target molecules and promote interfacial mass/electron transport. Lately, PtCu$_3$ nanocages were synthesized, which worked as a horseradish peroxidase (HRP)-like nanozyme and GSH-Px, and both of them are beneficial to cancer therapy (Fig. 4F–H).[63] Also, GSH-depleted PtCu$_3$ nanocages performed as a sonosensitizer, displaying high production rate of reactive oxygen species (ROS) upon US irradiation. Owing to the

fantastic properties of metallic nanoframes, our research group also prepared 3D open-structured PtCu nanoframes and rhombic dodecahedral Cu_3Pt nanoframes, and explored their applications in electrochemical immunosensing systems.[64,65]

It is known that hollow Au-based nanomaterials show strong interactions with light and surrounding media, on account of their larger surface area than that of solid particles, showing great promise for establishing sensitive NIR sensors. Recently, dual Pt@Au nanoring@DNA probes were developed for fluorescence (FL) imaging and PTT of tumor cells (Fig. 4I and J).[66] Also, Au–Ag hollow nanotriangles (Au–Ag HTNs) have great surface-to-volume ratio, sharp edges and vertices, along with a unique local curvature relative to other Au–Ag NPs, thus displaying strong absorption in the NIR-II region (Fig. 4K).[67] As the Au–Ag HTNs were further immobilized with glucose oxidase (GOx), they effectively promoted a plasmon-accelerated cascade reaction for high-efficiency tumor therapy.

2.5 Surface modification

Apart from the shape, size, composition and structure, the properties of HMNMs also correlate with surface properties. Generally, surface modification strategies include surface engineering (e.g. coating with a polymer, silane, dendrimers and/or other metal(s)), attachment of functional groups to block surface access, and regulation of electronic structure and surface acidity, which in turn improve the activity, stability, specificity and biocompatibility.[44,63,68]

Coating HMNM surfaces with a polymer makes them less toxic and more biocompatible. Notably, modification of HMNMs with hydrophilic polymers is instructive to improve their dispersibility, combined with their efficient conjugation with biomolecules, which is the key step in sensing, drug delivery, and therapeutic applications.[20,29,69,70] Nevertheless, it is difficult to achieve such conjugations in many cases, except by initially coating with an appropriate linker. For example, thiolated polyethylene glycol (SH-PEG) acted as a linker for porous Au@Pt NPs to effectively load anticancer drug DOX, and further functionalization with the cRGD peptide, eventually showing significant improvement in colloidal stability and targeting property.[29]

By scalable functionalization with more specific ligands, selectivity can be greatly improved for different target molecules in such nanosystems.[29,71] Plainly, folic acid (FA) is a feasible endocytic ligand for folate receptors that are overexpressed in diverse human cancer cells, and hence displays high affinity towards cancer cells.[20,32,71] For instance, Au eyeball-like NPs with open-mouthed Pd shells (Au@Pd) were prepared and further modified with FA for cell-targeting and Chlorin e6 (Ce6), which led to their selective accumulation at the tumor site and effective triggering of cell apoptosis as a photodynamic agent.[71] Similarly, Au_3Cu tetrapod nanocrystals (TPNCs) were synthesized and immobilized with PEG, Cy5 and FA, endowing the Au_3Cu TPNCs with superior physical stability, FL imaging effect, and accurate targeting ability for multi-modal image-guided PTT, by adopting multispectral photoacoustic tomography (MSOT) imaging.[20] In addition, an Au/Pt star-shaped core (Au/Pt

star) was successively combined with L-cysteine by covalently linking cystamine dihydrochloride and targeted ligand rHSA-FA, followed by physical adsorption of a NIR fluorophore (IR780) and GOx.[32] The resulting composite accelerates GSH-triggered sequential catalysis for tumor imaging and eradication based on the star-like Au/Pt enzyme carrier system.

Also, BSA is a commonly used protective molecule in various probes and sensor designs, which can prevent non-specific adsorption and improve specificity and biocompatibility accordingly.[49,64,72,73] For example, Au nanobipyramid cores with external silver nanorods were prepared, and subsequently coated with 4-mercaptobenzoicacid (4-MBA), FA and reduced bovine serum albumin (rBSA).[74] The hybrid nanoprobes had appealing specificity and biocompatibility with living gastric cancer cells (MGC-803) due to the conjugation of FA and modification of rBSA that can effectively avoid non-specific attachment of non-targeted cells. In the same way, single-signal and dual-signal ratio immunosensors were separately built based on reduced graphene oxide (rGO)-polydopamine-grafted-ferrocene/Au@Ag nanoshuttles and hollow Ni@PtNi yolk–shell nanocages-thionine (Ni@PtNi HNCs)[37] as well as PtCu hollow nanoframes,[55] where BSA performed as a sealing agent in the construction of the biosensors.

By virtue of high specificity of the A–T and G–C hydrogen-bonded Watson–Crick interactions, coupled with superior biocompatibility and scalable designability, DNA has achieved success in construction of diverse nanostructures and its practical application in biological analysis.[75] In this regard, NIR light-activated Pt@Au nanoring@DNA probes were designed for FL imaging and targeted PTT of cancer cells, owing to fine regulation of specific recognition and imaging by dehybridization of double-stranded DNA (dsDNA), combined with temperature variation upon NIR light irradiation.[66] Also, amino-terminated AS1411 formed G-quadruplex structures on Pt-based nanostructures via Hoogsteen hydrogen bonds. To this end, an enzyme-free electrochemical biosensor was developed based on PdRu/Pt heterostructures, integrated with hemin/G-quadruplex as a signal magnification probe, which finally showed efficient determination of circulating tumor cells (CTCs).[76]

Small molecules (e.g. Cys and GSH) have hydrophilic groups such as amine and carboxyl groups, which improve solubility of HMNMs in aqueous media, ultimately realizing good dispersibility of HMNMs.[9,77] Lately, ultra-small Cys-coated FePd bimetallic nanodots showed a negative zeta potential of −45.4 mV, and still remained uniform in phosphate buffer solution (PBS) and serum samples even after immersion for 24 h, reflecting their good biocompatibility and excellent stability, unlike pure FePd counterpart which already deposited at the bottle bottom. Both the in vitro and in vivo results certify Cys–FePd nanodots as a feasible contrast agent for tri-modal CT/MR/PA imaging and hypoxia-resistant thermo-RT in a NIR-II scope.[8]

By the same token, GSH capped Au–Bi NPs were prepared and further immobilized with IR808 dye through sulfate and carboxylic groups of GSH (termed Au–Bi-GSH@IR808 for clarity). Such a hybrid composite showed good-dispersion in an

aqueous environment (due to GSH ligands) and prominent CT imaging property, and noticeably enhanced therapeutic effect in accurate diagnosis and treatment of cancer.[77]

Last but not least, photosensitizer ICG was efficiently loaded and retained in the cavity of a porous Au@Rh biphasic core–shell nanostructure (denoted as Au@Rh-ICG). The Au@Rh-ICG was further grafted with the tumor CM *via* homologous binding. The resulting nanocomposite behaved as an H_2O_2-driven oxygenerator to alleviate tumor hypoxia for simultaneous bimodal imaging and enhanced PDT, and showed large tumor accumulation and high biocompatibility, along with superior FL and PA imaging properties.[28]

2.6   Construction of hybrid nanomaterials

In general, HMNMs exhibit superior catalytic activity due to the synergistic effects between different metals and unique structures.[7,42] Alternatively, single particles tend to agglomerate together due to large surface energy, and consequently reduce the effective surface area and weaken the catalytic properties.[78–82] To address this issue, many materials such as carbon materials,[78,79,83–93] metal oxides,[80–82,94–107] and sulfides,[108–111] as well as metal organic frameworks (MOFs, consisting of organic ligands and metal ions)[112–114] have been explored as supports or wrapping materials recently. Among them, there are many carbon- and metal-oxide based hybrid nanomaterials, showing

Table 1 Hybrid materials based on carbon materials and oxides, and their typical applications

Hybrid nanomaterials	Applications	Ref.
AgPt–rGO	CEA	83
Au@Pt/GO	H_2O_2	84
PtCu@rGO/g-C_3N_4	PSA	85
FePt/GO	MR/CT imaging	86
Cu–Ag/rGO	Glucose and ascorbic acid	87
PtPd/N-GQDs@Au	CEA	88
Pd@Au@Pt/COOH-rGO	CEA and PSA	89
3D graphene/AuPtPd	ctDNA	78
Au–Pd/GO	H_2O_2	90
HAC-AuPt	ctDNA	91
PdCu/CB	H_2O_2	92
PdFe/GDY	GSH detection and antibacterial	93
SWCNT/Ag/Au	SERS imaging of hypoxia	79
AuAg@p-SiO$_2$	H_2O_2	94
Au–Pt/SiO$_2$	H_2O_2	95
Au/Gd@SiO$_2$	MSCs	80
Fe$_3$O$_4$@SiO$_2$–Au@Pd$_{0.30}$	Glucose	96
FePt/SiO$_2$/Au	PTT and MRI imaging	97
Au@Ag@SiO$_2$	AFP	98
Co/Fe–MSNs	Cysteine	99
SiO$_2$@Au@Ag	PSA	81
AuPd@Fe$_x$O$_y$	CDT–PTT	100
Fe$_3$O$_4$@Au@Ag	IgG	101
Au@Pd/NH$_2$–MoO$_2$	HBsAg	102
MnO$_2$@PtCo	Hypoxic tumors	82
MnO$_2$/Au@Pd^Pt	NSE	103
Ag–Au–TiO$_2$	Photocatalytic and antimicrobial	104
Cu$_2$O@PtPd	Early cell apoptosis	105
Au–Ag/Co$_3$O$_4$	H_2O_2	106
Co$_3$O$_4$@CeO$_2$–Au@Pt	SCCA	107

broad applications in sensing and analysis (Table 1).[78–107] For example, a seed-mediated approach was developed for aqueous synthesis of heterodimeric structures such as AgPt$_{alloy}$–Fe$_3$O$_4$ and Au$_{core}$@Pd$_{shell}$–Fe$_3$O$_4$,[115] and they were adopted as excellent contrast agents in imaging modalities such as optical coherence tomography (OCT) and PA with excellent performances.

Recently, graphene[116] and other 2D transition metal dichalcogenides (TMDCs) have found widespread applications in versatile electronic and optoelectronic applications, owing to their unique optical, electrical and mechanical properties.[117] Particularly, TMDCs such as MoS$_2$ display a mono-layered unique structure, large specific surface area, high catalytic activity, good electrical and optical properties, integrated with high mechanical flexibility.[108,109] Generally, they worked as ideal alternatives to replace the state-of-the-art silicon-based technology.[118] Incorporation of HMNMs such as PtPd nanocubes in MoS$_2$ nanosheets (PtPd NCs@MoS$_2$) largely improved electronic conductivity and produced more reaction sites, showing accelerated POD-like activity by contrast with PtPd NCs and MoS$_2$ alone.[108] Zhao and co-workers prepared Au–Pd–Pt nanoflower modified MoS$_2$ nanosheets (Au–Pd–Pt/MoS$_2$) as a co-reaction accelerator for building an ECL immunosensor to detect cystatin C (CYSC), and they showed a wide linear range and low limit of detection (LOD).[109]

It is noteworthy that HMNMs are certified to show distinct enhancement in the photocurrents of photoactive materials, due to the localized surface plasmon resonance (LSPR) effect.[119] Besides, typical Schottky junctions are formed by fine integration of noble metals and photoactive materials, showing robust improvement in the transport and separation of photoinduced carriers.[111] For instance, ultrasensitive split-type and GOx-mediated photoelectrochemical (PEC) immunoanalysis was developed for CEA assay by employing photoactive CdS nanorods combined with PdPt nanozyme.[110] Also, Jin *et al.* chose GOx and alkaline phosphatase (ALP) to prepare core–shell CdSe/ZnS@Au hybrid nanostructures.[111]

As already reported, MOFs show a remarkable increase in loading capacity, thanks to the large specific surface area, scalable porosity, facile surface modification, good stability, and mild synthesis conditions.[120] MOFs have wide applications in biosensing, analysis and therapy.[121] For instance, iron-porphyrinic MOFs (PCN-223-Fe) were synthesized with Zr^{4+} and iron-porphyrin (as a linker), and then *in situ* located with spindle-shaped PtAg NPs, followed by exploring them to build an electrochemical aptasensor for ultrasensitive assay of OTA.[112]

3.   Applications of HMNMs in analytical chemistry

3.1   Sensing

By contrast with MMNMs, HMNMs have gained tremendous research focus due to their intrinsic properties such as superior biocompatibility, good electrical conductivity, and extremely high catalytic activity.[7,8] To date, HMNM-based biosensing devices are continuously built and applied in determination of

metal ions, small molecules, proteins, nucleic acids, and cancer cells.[24,76,78,96,122–124]

3.1.1 Metal ions. Recently, environmental pollution induced by heavy metals (*e.g.* Hg^{2+}, Cd^{2+} and Pb^{2+}) has attracted increasing concern with rapid development of the world's economy.[17] Heavy metals ions are not easily degradable, and they remain and accumulate in the ecosystem and food chains, leading to serious human health problems even at trace levels.[17] Therefore, it is important yet imperative to sensitively detect heavy metal ions in water and food with the purpose to protect the environment and human health.

Specifically, Hg^{2+} is one of heavy metal ions with wide applications in industry and agriculture, whose strong toxicity and bioaccumulation even at very low concentrations can cause tumor, neural disorder, kidney damage, and epithermal tissue damage.[125] As a result, various methods have been developed for its assay in the last decades.[126,127] Recently, Au@Pt NPs[122] and Ag–Cu NPs[128] were prepared for sensitive detection of Hg^{2+}. Later on, a Ag–Fe bimetallic-3-(trimethoxysilyl) propyl methacrylate framework was synthesized as a colorimetric probe for determination of Hg^{2+}, and further applied for efficient analysis of Hg^{2+} in different environmental aqueous media.[129]

As an extremely toxic metal, Cd^{2+} frequently exists in agriculture and industry, and can induce different lesions and diseases (*e.g.* pulmonary edema, emphysema, pneumonitis and even cancer).[130] Therefore, many economical and effective approaches have been developed for its qualitative and quantitative analysis.[123,131] For instance, a femtosecond laser processing technique was developed for selective formation of layered Cu–Ag nanodots within glass microfluidic channels, combined with electroless plating.[123] In the presence of crystal violet, Rhodamine 6G was detected on the resulting SERS microfluidic chip with an enhancement factor of 7.3×10^8 and a relative standard deviation of 8.88%, followed by achieving real-time assay of Cd^{2+} down to 10 ppb.

In addition, Pb^{2+} is recognized as a major, ubiquitous and bioaccumulative heavy metal pollutant in environment and food.[132] It is harmful to kidneys and brain even at a very low concentration, and hence many strategies have been designed for its detection recently.[132,133] For example, Au@Pt NPs were prepared by deposition of Pt onto Au NPs, and they served as a nanozyme for colorimetric determination of Pb^{2+} leaching from a Pb^{2+}–$S_2O_3^{2-}$ system with a linear range of $20 \sim 800$ nM, as well as high sensitivity and selectivity.[133]

3.1.2 Small molecules. Many diseases have close relationship with human aging, while the insights into basic molecular mechanisms associated with aging, age-related diseases, and oxidative stress still remain insufficient.[134] Particularly, oxidative stress stems from unregulated formation of ROS and cellular mismanagement of redox reactions to trigger follow-up oxidative damage to tissues and organs, where H_2O_2 is a main ROS and a common marker to evaluate oxidative stress in living organisms.[135] Therefore, detection of H_2O_2 plays a vital role in pharmaceutical and clinical analysis, combined with enhancing our understanding of H_2O_2 physiology and pathology.[136]

To date, a variety of HMNM-associated sensors have been constructed for H_2O_2 detection, including SERS,[94,124] colorimetric detection,[84,95,137] and electrochemical sensing.[92,106] For example, ultra-thin porous silica shell-coated Au–Ag alloy NPs (AuAg@p-SiO$_2$) were synthesized and immobilized with 4-mercaptophenylboronic acid (MPBA) and 4-mercaptophenylacetylene (MPAE, 1986 cm^{-1}) as internal standard. After incubation with dopamine (DA), the bridging molecules were grafted on the particle surface *via* a borate bond between DA and MPBA, followed by conjugating 3-(4-(phenylethynyl) benzylthio) propanoic acid (PEB, 2214 cm^{-1}) as signaling alkyne molecules *via* an amide bond between the carboxyl group on the PEB and the amino group on the DA, eventually forming a ratiometric SERS nanoprobe for Raman imaging of H_2O_2 in living cells.[94] The Raman signals at 2214 cm^{-1} were significantly decayed with H_2O_2 when the alkynyl on the PEB was released from the particle surface, while that of MPAE at 1986 cm^{-1} remained unchanged. Thus, quantitative analysis of H_2O_2 concentration was realized according to the ratiometric value of I_{1986}/I_{2214} in a linear scope of $0.12 \sim 8$ μM, with a LOD as low as 52 nM (S/N = 3).

In another case, FePt–Au NPs were prepared by a seed-mediated hydrothermal approach, and they can oxidize 3,3′,5,5′-tetramethylbenzidine (TMB) to a blue product, eventually developing a colorimetric sensor for fast detection of H_2O_2.[137] What's more, a PdCu NP/carbon black (CB) based electrochemical biosensor was fabricated for sensitively detecting H_2O_2 released from live cells.[92]

Similarly, glucose is an important chemical substance correlated to nervous system, so its determination is essential[138] and rational when HMNMs are integrated with GOx by utilizing the intrinsic POD-like ability.[96,139] For example, Au@Pd NPs were efficiently decorated on a nanomagnet-silica shell (Fe$_3$-O$_4$@SiO$_2$), which showed superior POD-like activity for TMB oxidation in the presence of H_2O_2.[96] Besides, a simple colorimetric sensor was established after physical adsorption of GOx, showing high selectivity and sensitivity for detecting glucose. In another instance, Pd nanosheet-supported Au NPs were synthesized by galvanic replacement, and further applied for sensitive glucose sensing based on their high catalysis towards TMB oxidation.[139]

Aside from H_2O_2 and glucose, HMNMs were also utilized for analysis of other molecules, including ascorbic acid,[87] biothiol,[93,99] hydrazine,[140] dibutyl phthalate,[141] adenosine,[142,143] ractopamine,[144] chloramphenicol,[145] hydroquinone,[146] malathion,[147] nitrite,[148] Sudan I,[149] and tetrabromobisphenol A.[150]

3.1.3 Proteins. As we all know, proteins are vital biomolecules that function as working units in living organisms and are involved in many aspects of life ranging from energy storage and metabolism to regulation of cell functions.[151] Some diseases frequently have close association with emergence of target proteins as biomarkers or their abnormal expression levels.[152] For early disease diagnosis, protein biomarkers usually stem from diseased cells themselves or others in response to the diseases, and are usually found in blood and sometimes in urine.[152,153] To date, researchers have developed a variety of HMNM-based electrochemical, FL and colorimetric biosensors to detect disease-related protein markers, such as tumor,

Table 2 HMNM-based immunosensors for the detection of protein biomarkers

Nanomaterials	Protein markers	Linear range	LOD	Ref.
Au@Pt/Au	p53 peptide	50–1000 nM	66 nM	154
Cu_3Pt	AFP	$0.1–10^4$ pg mL^{-1}	0.033 pg mL^{-1}	65
Au@Pt/MoSe$_2$	AFP	$10–2 \times 10^8$ fg mL^{-1}	3.3 fg mL^{-1}	155
Au@Ag	AFP	0.5–100 pg mL^{-1}	0.081 pg mL^{-1}	156
AuNS@Ag@SiO$_2$	AFP	$3–3 \times 10^6$ pg mL^{-1}	0.72 pg mL^{-1}	98
PtCo	CA153	0.1–200 U mL^{-1}	0.0114 U mL^{-1}	36
AuPt	CA199	0.05–50 U mL^{-1}	0.03 U mL^{-1}	157
Au@Pt	CA153	0.5–200 U mL^{-1}	0.17 U mL^{-1}	158
AuAg	CA199	1–30 U mL^{-1}	0.228 U mL^{-1}	159
Au–Ag	CA125	$5 \times 10^{-4}–1$ U mL^{-1}	5×10^{-5} U mL^{-1}	24
AgPt	CEA	$5–5 \times 10^7$ fg mL^{-1}	1.43 fg mL^{-1}	84
PtPd/N-GQDs@Au	CEA	$5–5 \times 10^7$ fg mL^{-1}	2 fg mL^{-1}	88
PdAuCu	CEA	0.001–100 ng mL^{-1}	0.23 pg mL^{-1}	52
MoS$_2$/Au@AgPt	CEA	$10–10^8$ fg mL^{-1}	3.09 fg mL^{-1}	160
Au@PtPd	CEA	$50–10^8$ fg mL^{-1}	16.7 fg mL^{-1}	30
CdS/PdPt	CEA	$1–5 \times 10^3$ pg mL^{-1}	0.21 pg mL^{-1}	110
Au@Pt	CEA	0.025–1.6 ng mL^{-1}	0.021 ng mL^{-1}	122
Ni–Pt	CEA	5–500 pg mL^{-1}	1.1 pg mL^{-1}	161
PtCu@rGO/g-C$_3$N$_4$	PSA	$50–4 \times 10^7$ fg mL^{-1}	16.6 fg mL^{-1}	85
AuPd@Au	PSA	0.1–50 ng mL^{-1}	0.078 ng mL^{-1}	162
Au@Pt	PSA	0.1–50 ng mL^{-1}	0.018 ng mL^{-1}	163
AuPtAg	PSA	0.05–50 ng mL^{-1}	0.017 ng mL^{-1}	164
PtCu	PSA	0.01–100 ng mL^{-1}	0.003 ng mL^{-1}	64
Au/Ag	PSA	10–200 ng mL^{-1}	1.53 ng mL^{-1}	165
Au@Ag	PSA	5–120 fg mL^{-1}	0.94 fg mL^{-1}	166
SiO$_2$@Au@Ag	PSA	2.5–25 ng mL^{-1}	0.006 ng mL^{-1}	81
rGO/Thi/AuPt and Au@Pd	NSE	0.0001–50 ng mL^{-1}	0.03 pg mL^{-1}	167
MnO$_2$/Au@Pd^Pt	NSE	$10–10^8$ fg mL^{-1}	4.17 fg mL^{-1}	103
Au@Pd	CFP-10	$5 \times 10^{-13}–5 \times 10^{-4}$ g mL^{-1}	5.6×10^{-12} g mL^{-1}	168
PdPtCoNi@Pt	CK-MB	0.001–2500 ng mL^{-1}	0.62 pg mL^{-1}	46
AuPdCu	CK-MB	0.001–2000 ng mL^{-1}	0.88 pg mL^{-1}	50
		$12–8.5 \times 10^4$ pg mL^{-1}	8 pg mL^{-1}	
Pd@Au@Pt/COOH–rGO	CEA/PSA	$3–6 \times 10^4$ pg mL^{-1}	2 pg mL^{-1}	89
PtCoCuPd	cTnI	0.001–100 ng mL^{-1}	0.2 pg mL^{-1}	47
NH$_2$-MIL-88B(Fe$_2$Co)-MOF	cTnI	$0.1–10 \times 10^7$ fg mL^{-1}	13 fg mL^{-1}	169
Au–Pd–Pt/MoS$_2$	CYSC	$1–5 \times 10^6$ fg mL^{-1}	0.35 fg mL^{-1}	109
Au/Ag	DNase I	0–80 unit mL^{-1}	0.056 unit mL^{-1}	170
PtPd@MoS$_2$	HBs Ag	$32–10^8$ fg mL^{-1}	10.2 fg mL^{-1}	108
Au@Pd–MoO$_2$	HBs Ag	$10–10^8$ fg mL^{-1}	3.3 fg mL^{-1}	102
AgPtCo	HE4	0.001–50 ng mL^{-1}	0.487 pg mL^{-1}	35
Au@Ag and Ni@PtNi	HER2	0.01–100 ng mL^{-1}	3.3 pg mL^{-1}	49
Au–Ag	IgG	0.89–1000 pM	0.89 pM	171
Fe$_3$O$_4$@Au@Ag	IgG	$1–10^6$ pg mL^{-1}	1 pg mL^{-1}	101
Au@Ag	Albumin	10–300 mg L^{-1}	0.2 mg L^{-1}	172
MOFs/AuPt	LAG-3 protein	$0.01–10^3$ ng mL^{-1}	1.1 pg mL^{-1}	114
Au@Pt	MMP-2	0.5–100 ng mL^{-1}	0.18 ng mL^{-1}	173
PtCoNi	NT-proBNP	0.001–10 ng mL^{-1}	0.35 pg mL^{-1}	51
Pd@PtRh	PCT	$20–10^8$ fg mL^{-1}	6.74 fg mL^{-1}	174
PtCoIr	PCT	0.001–100 ng mL^{-1}	0.46 pg mL^{-1}	175
Au@Pt	SARS-CoV-2	10–100 ng mL^{-1}	11 ng mL^{-1}	176
Co–Fe@hemin	SARS-CoV-2	0.2–100 ng mL^{-1}	0.1 ng mL^{-1}	177
Au@Ag	SCCA	2.5–115 ng mL^{-1}	0.85 ng mL^{-1}	178
Co$_3$O$_4$@CeO$_2$–Au@Pt	SCCA	$0.1–8 \times 10^4$ pg mL^{-1}	33 fg mL^{-1}	107

hepatic, cardiac, inflammatory markers, and others (Table 2).[24,30,35,36,46,47,49–52,64,65,81,84,85,88,89,98,101–103,107–110,114,122,154–178]

3.1.4 Nucleic acids. Circulating tumor DNA (ctDNA) is an informative cancer biomarker, which has genetic changes and the same mutations as primary tumor, even behaving as a "liquid biopsy" for early tumor discovery and hence avoiding traditional tissue biopsy.[179] For example, AuPt alloyed NPs were

efficiently synthesized and loaded on high-active carbon (HAC) for reducing H$_2$O$_2$, and they showed significantly amplified electrochemical signals on the as-built ctDNA biosensor.[91] Also, a graphene/AuPtPd nanoflower-based sensor was built for highly specific and accurate analysis of trace ctDNA in human serum samples, showing substantial promise for sensitive assay of ctDNA in clinical and diagnostic applications.[78]

MicroRNAs (miRNAs), as a group of small molecules, consist of 18–22 nucleotide long noncoding RNA, and play a decisive role in RNA silencing and regulation of gene expression upon reverse transcription.[180] Their varied expression would correlate with abnormal conditions such as suboptimal growth and diseases (*e.g.* cardiovascular disease, Alzheimer's disease, skin disease, and cancer), and they work as biomarkers in pathophysiological environments for determining the onset and prognosis of diseases in clinical diagnosis.[181]

For instance, mesoporous Au–Ag alloy films were prepared *via* electrochemical micelle assembly, and they showed high catalytic activity towards redox reaction of $[Fe(CN)_6]^{3-/4-}$ and were used to build a miRNA sensor with a low LOD.[182] By bifacial regulation of Ag–Au nanocages and subsequent deposition of DNAzyme-motif nanobrushes on the external cage surface, a hollow Janus hybrid nanozyme was designed towards SERS liquid biopsy at nano-/micro-scales, due to improved POD-like activity.[58] Likewise, PtCuCo triM alloys were fabricated, which showed good catalytic activity in a luminol-H_2O_2 system towards determination of miRNA-21.[183]

3.1.5 Cancer cells. Quick identification and imaging of living cancer cells are important for cancer diagnosis, prognosis and treatment monitoring in clinic.[184] Nevertheless, accurate and rapid detection of living cancer cells is pivotal in early diagnosis and follow-up therapy in practice.[185] Recently, plenty of HMNMs have been widely applied for assay of cancer cells with accepted performances.[74,76,186]

Hemin/G-quadruplex DNAzyme was subtly integrated with Pt NPs decorated hyperbranched PdRu nanospines (PdRu NSs/Pt), and they displayed simultaneous catalysis of H_2O_2 to achieve multiplexed signal magnification, confirming feasibility for analysis of model CTCs with a LOD as low as 2 cell mL^{-1}.[76] Meanwhile, BSA coated Bi/Pt NPs (BSA-Bi/Pt) exhibited highly boosted POD mimicking activity in comparison with BSA-Pt NPs, combined with largely improved stability in harsh surroundings (*e.g.* high temperature, extreme pH environment, and high ionic strength), and a complicated biological matrix, realizing efficient assay of cancer cells (*e.g.* MCF-7) through the target recognition function of FA.[186]

Apart from the above, other representative examples include inner Au nanobipyramids and external Ag nanorods as a substrate for building a SERS biosensor,[74] and Cu$_2$-O@PtPd for constructing an amperometric cytosensor.[105] These examples certify their promising potential for early evaluation of cancers and even therapeutic effect of anti-cancer drugs in clinic.

3.2 Imaging

HMNMs demonstrate substantial potential as radiosensitizers for enhancement of RT in biomedical applications.[187,188] They have been widely adopted in imaging to promote development of sensing, catalysis, diagnosis and therapy, in which many techniques such as photoluminescence (PL), ECL, FL, Raman, MR, CT and PA microscopy are involved.[25,55,63,170,189,190] This section only gives some typical examples of different imaging applications.

3.2.1 PL imaging. PL imaging is a powerful tool extensively employed in biosensing and bioimaging, attributing to their distinct advantages such as weaker photo-damage, non-invasiveness, and high sensitivity as well as excellent temporal and spatial resolution.[191,192] For example, Au and Ag nanospheres were agglomerated together, showing large improvement of two-photon photoluminescence (2PPL), due to their LSPR property and plasmonic coupling effect.[191,193] As well, Au@Ag NPs displayed giant 2PPL upon aggregation, demonstrating two-photon imaging of bacteria under NIR femtosecond laser pulses.[189]

Combined with near-field modeling, far-field spectroscopy is frequently adopted to investigate optical properties of the plasmonic structures based on the near-field interactions.[194,195] By contrast, far- and near-field spectral responses are certified to have lots of important applications.[196,197] For instance, Halas *et al.* exhibited spatial and spectral mapping of optical forces between nanotips and Au–Al nanodisk heterodimers by photo-induced force microscopy (Fig. 5A–F).[197] They found that near-field coupling derived from nanoscale gaps accounts for inter-particle interactions.

Beyond the above, ECL is a potential initiated form of chemiluminescence, and offers opportunity for an optical readout in catalysis, sensing and analysis, where luminophores are oxidized or reduced at the electrode surface and yield emissive excited-state species.[198–200] For instance, ECL microscopy was applied to characterize electro–catalytic activity of Au–Pt JNPs (Fig. 5G–I).[55] In comparison with single particles, Au–Pt JNPs largely boosted the osmotic gradient during electrocatalytic oxidation of Ru(bpy)$_3^{2+}$ due to their directionality and asymmetry, and effectively prevented the formation of individual Au and Pt oxides, ultimately improving the ECL stability of Au–Pt JNPs compared to single counterparts.[201]

3.2.2 FL imaging. FL imaging, as a safe and noninvasive biological imaging technique with high resolution and sensitivity, is an important tool to investigate molecular structures and interactions, location and dynamics of gene expression, and protein expression in cells and even tissues, combined by monitoring therapeutic procedures and residual diseases.[202] It mainly takes advantage of photons emitted from fluorescent probes (*e.g.* dyes and proteins). Recently, fluorescent nanoprobes have broad applications in imaging proteins for chemical sensing and clinical therapies, where a Au–S-bond-based probe is the most popular due to its simple preparation and operation, even though it is easily damaged by intracellular GSH.[203]

To overcome this problem, a Au–Se nanoplatform was developed by combining Se-modified peptides with Au NPs, and it exhibits excellent anti-interference property and high-fidelity fluorescence signals even in physiological systems, enabling the monitoring of changes of caspase-9 in MCF-7 cells by treating with staurosporine.[190] After that, an Au–Se-bonded nanoprobe was developed for monitoring urokinase-type plasminogen activator (uPA) and matrix metalloproteinase-9 (MMP-9) in MCF cells, achieving real-time *in situ* imaging of their dynamic changes and regulatory correlations.[204] Specifically, Au NPs were conjugated with two Se-modified peptide chains initially grafted
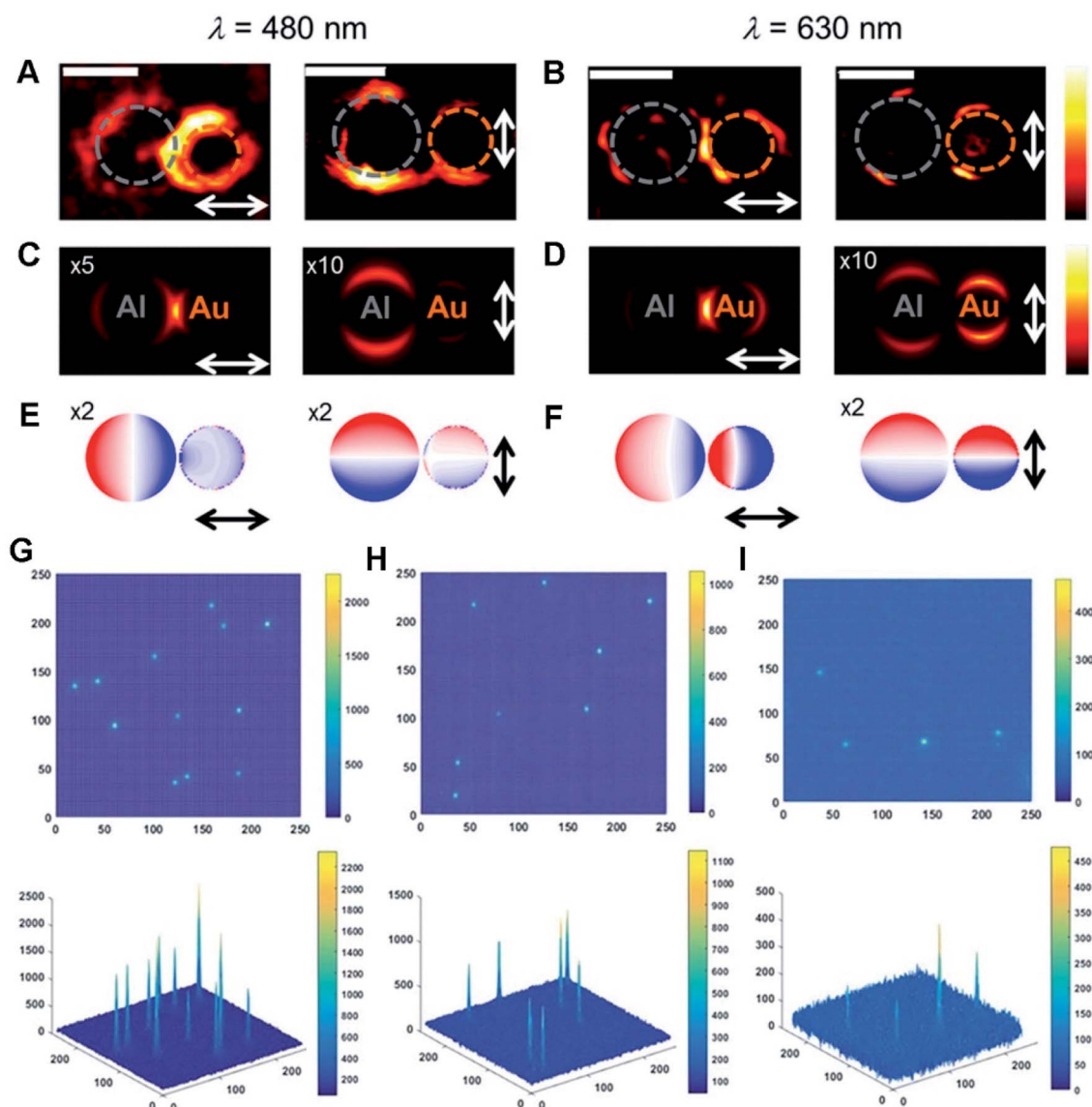
Fig. 5 (A and B) Photoinduced force maps of Al−Au heterodimer structures using Si tips (gap size = 5 nm). (C and D) Photoinduced force maps of the heterodimer structures (Al disc d = 92 nm, Au disc d = 66 nm, and gap size = 5 nm). (E and F) Corresponding surface charge plots in the heterodimer structures. The arrows display the direction of in-plane polarization. Scale bars: 100 nm. Reproduced with permission.[197] Copyright 2018, American Chemical Society. 2D and 3D ECL intensity diagrams of (G) Au−Pt JNPs, (H) Pt NPs, and (I) Au NPs. Reproduced with permission.[55] Copyright 2018, Wiley.

with 5-aminomethyl Rhodamine (5-TAMRA) and fluorescein isothiocyanate (FITC). The anchored peptide chains are selectively cleaved after contacting with uPA and MMP-9, finally recovering the FL. Further, the functional Au−Se probe was utilized to monitor lipopolysaccharide (LPS)-treated cancer cell imaging, and the FL for uPA emerged early, reflecting that uPA worked upstream of MMP-9. Overall, the aforementioned research provides visual determination methods of the biomarkers to monitor invasive potential of breast cancer cells by *in situ* FL imaging of uPA and/or MMP-2 proteins and evaluate degree of breast cancer malignancy, combined with illustrating correlations among signal molecules of other signaling pathways in future.[205]

With continuous research advancement, HMNM-based FL imaging displays potential for application in clinical practice to monitor treatment procedures of cancers.[32,66,77,206] For example, core−shell Au/Pt star based multifunctional nanoprobes were successfully constructed upon conjugation with a GSH-sensitive S−S bond, a targeting ligand (rHSA-FA), a NIR fluorophore (IR780) and GOx. The IR780 molecules were released *via* cleavage of disulfide linker by GSH in cells, followed by sequential GSH-triggered catalysis for real-time tumor imaging and PTT&PDT.[32]

Also, Au@Pt NPs were successively modified with a mitochondrion-targeting triphenylphosphine (TPP) group, a cell-targeting ligand (FA), and a photosensitizer (Ce6), and they

further worked as a platform for rapid uptake of multifunctional mesopores by mitochondria in cells.[206] As confirmed by FL imaging, the as-formed Au@Pt NPs showed substantial enhancement in the PDT effect and conversion of laser radiation into heat, and thermally induced MCF-7 cell damage, in turn boosting therapeutic efficiency. Overall, the above nanosystems behaved as scalable phototherapeutic agents for significantly enhanced cancer therapy and molecular targets associated with disease progression.

3.2.3 SERS imaging. Recently, SERS tags have wide applications in cancer imaging. Importantly, SERS imaging has many advantages compared to FL imaging, including no photobleaching, narrow emission peaks, and negligible phototoxicity, coupled by reduction of the interference of autofluorescence and damage to cells in biological samples.[207,208] In view of the above characteristics, HMNM based Raman probes have been broadly applied in sensing,[60,209] imaging,[79,170] drug delivery,[210] and therapy.[211]

As known, Au- and Ag-based HMNMs are most frequently used as SERS-active substrates, owing to their superior plasmonic properties, high chemical stability, and low cytotoxicity.[170,209,211] For instance, alloyed Au/Ag NPs acted as a SERS substrate for quantitative analysis of endonuclease *via* modification with 4-thiophenylacetylene (4-TPA, as the internal

standard molecule) and single-stranded DNA (ssDNA) carrying 3-[4-(phenylethynyl)benzylthio]propanoic acid (PEB, as the reporter molecule), as revealed in Fig. 6A–C.[170] Briefly, PEB molecules were released upon exposure to endonuclease, and thus the associated Raman peak at 2215 cm^{-1} became weak, on account of breakage of the ssDNA. Simultaneously, Raman peak at 1983 cm^{-1} from 4-TPA almost remained constant, and thereby determination of endonuclease was achieved with a LOD of 0.056 unit mL^{-1}, according to the ratio variations of the two peak intensities (I_{1983}/I_{2215}). Finally, SERS imaging was explored to monitor HeLa cells incubated with Au/Ag NPs during apoptosis, certifying the overexpression of endonucleases during the cell apoptotic process. In another case, Ag/Au alloy NPs were supported on SWCNTs initially assembled with azoalkynes, which were adopted for ratiometric SERS imaging of hypoxia with assistance of the Raman band from the alkyne and the 2D-band of SWCNTs.[79]

In order to improve chemical stability, Ag nanospheres were efficiently coated with Au shells by a stoichiometric method, and their chemical stability was evaluated with NaSH, H$_2$O$_2$, and H$_2$S gas.[209] The Ag@Au core/satellites exhibited 3-fold enhancement in SERS intensity relative to Ag core/satellites, and highly improved stability for SERS imaging (Fig. 6D). Besides, Au NPs behaved as the core, bridging Raman reporter
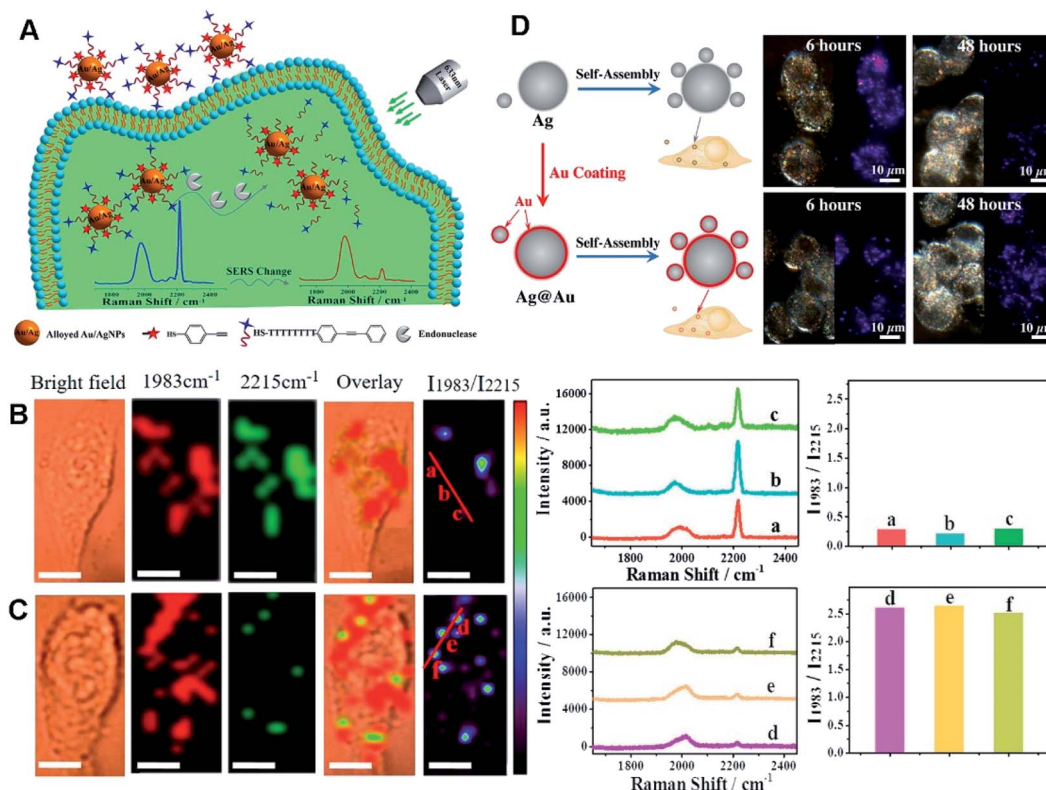

Fig. 6 (A) Schematic diagram of DNA-alkyne-modified Au/Ag NPs for ratiometric SERS detection of endonuclease. SERS imaging of HeLa cells incubated with the nanoprobe before (B) and after (C) incubation with PEITC. I_{1983}/I_{2215} Raman ratiometric images are presented in pseudocolor. Scale bar: 10 μm. SERS spectra and ratiometric peak were obtained from points (a–c) and (d–f). Reproduced with permission.[170] Copyright 2018, American Chemical Society. (D) Schematic diagram of the assembly process for Ag core/satellites and Ag@Au core/satellites. The corresponding dark field image and SERS mapping image of different probes at different times. Reproduced with permission.[209] Copyright 2017, American Chemical Society.

molecule 4-MBA and copper(II) carboxylate MOFs (Cu$_3$(BTC)$_2$) used as the shell for synthesis of core–shell Au@Cu$_3$(BTC)$_2$ NPs, showing feasible application in SERS imaging and chemo-phototherapy.[211] Specifically, inner Au NPs worked as photo-thermal agents and SERS-active substrates, and the external Cu$_3$(BTC)$_2$ shell was further linked with a specific aptamer for cell-targeting and loaded with an anticancer drug such as DOX,

finally showing an effective theranostic effect in chemo-PTT by a series of experiments.

3.2.4   CT imaging. CT imaging is a very important imaging tool because of its fine X-ray attenuation characteristics and deep penetration imaging of tissues, which can be performed with high resolution in biosamples.[119,212] So far, a series of nanomaterials (*e.g.* MMNMs, HMNMs, and carbon-based
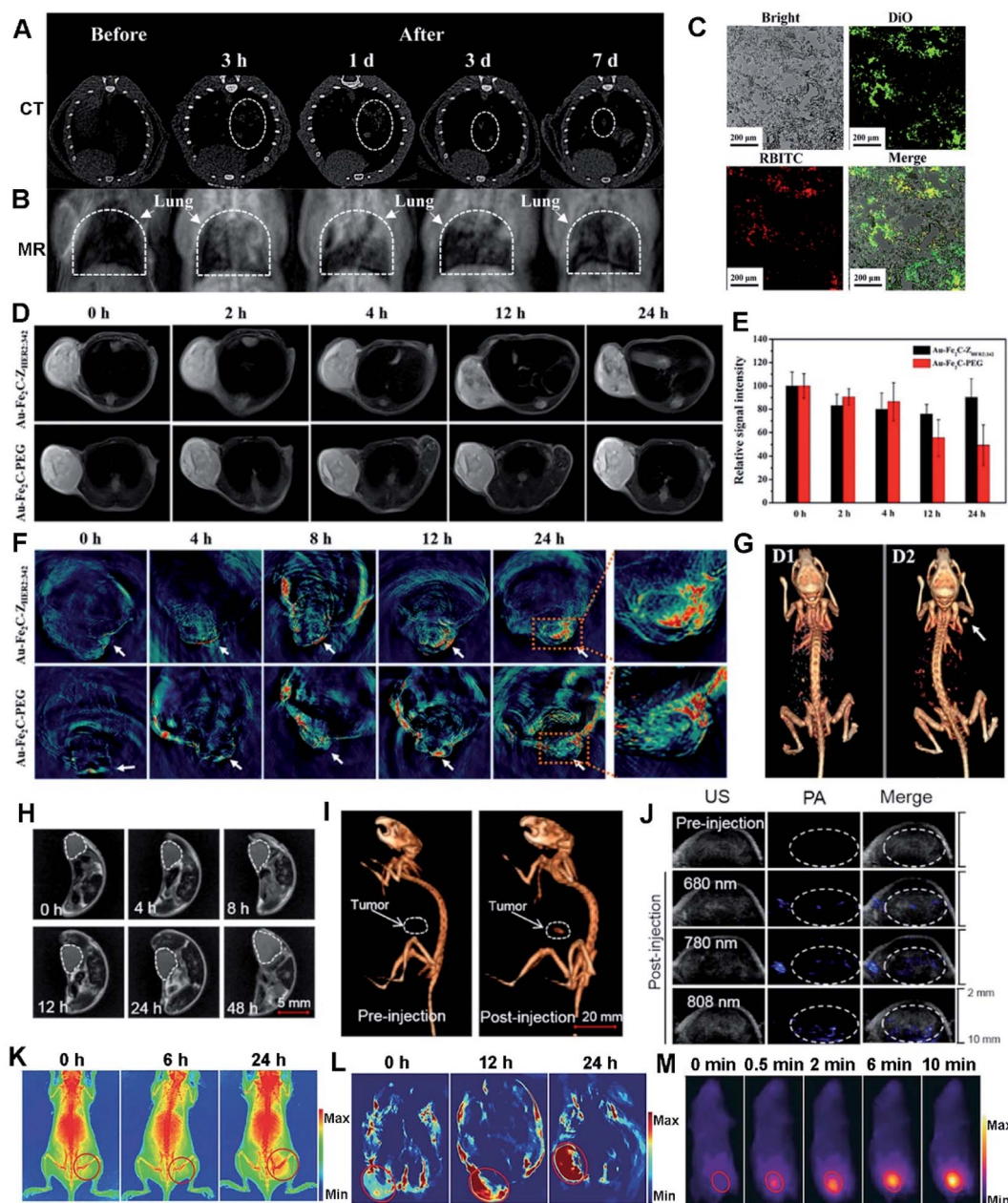

Fig. 7   CT (A) and MR (B) images of the Au/GdNC@SiO$_2$-labeled hMSCs in the lung of a pulmonary fibrosis mouse. (C) Fluorescence images of pulmonary frozen sections from the mouse. Reproduced with permission.[80] Copyright 2020, American Chemical Society. (D) Real-time T_2-weighted MR images of MDA-MB-231 tumor-bearing mice at different time points. (E) Relative MR intensity at different time points. (F) *In vivo* MSOT images of tumors in mice taken at different times. (G) 3D reconstructed CT images before (D1) and after (D2) the intratumor injection of Au−Fe$_2$C−PEG JNPs. Reproduced with permission.[56] Copyright 2017, American Chemical Society. (H) Tumoral accumulation of SeAuFe-EpC NPs within 48 h. (I) The 3D *in vivo* CT images of MCF-7 tumor-bearing mice before and after injection with SeAuFe-EpC NPs. (J) Representative photos of PA images of a mouse model before and after intravenous injection under different NIR wavelengths. Reproduced with permission.[188] Copyright 2020, Elsevier. Triple-modal imaging of mice after injection with TPAN at indicated time points. X-ray images (K), PA images (L), and IR thermal images (M) of the marked tumor areas. Reproduced with permission.[40] Copyright 2019, Wiley.

nanomaterials) have emerged as multifunctional theranostic and/or contrast nanoagents for improving efficiency of cancer therapy with development of nanotechnology.[56,213,214] To date, a variety of HMNMs have been explored for CT imaging and synergistic thermo-RT, and they significantly enhanced the output of CT imaging and therapeutic effect in the diagnosis and treatment of tumors, due to the synergistic effects in comparison with MMNMs.[19,25,26,214]

For example, ultrasmall Au–Ag@BSA NPs were obtained by utilizing BSA as a template, and they showed high stability, good dispersity and biocompatibility, as well as low cytotoxicity in A549 and MCF-7 cells.[25] Notably, the hybrid NPs with an Au/Ag molar ratio of 3 : 2 showed improved CT performance as a contrast agent in CT imaging of early-stage zebrafish embryos, surpassing Au NPs and iohexol. Inspired by the formation mechanism of gallstones, Au–Ag, Pt–Ag and Pd–Ag 3D supra-nanostructures were developed as contrast agents for medical CT imaging and radiosensitizers for image-guided radiation therapy.[214] In another example, PEGylated Au@Pt nano-dendrites were synthesized as CT contrast with significant enhancement in CT imaging signals and an improved theranostic agent for tumor therapy using PTT/RT.[26]

3.2.5 Multimode imaging. Multimodal imaging is favoured for tracking tumor occurrence, proliferation, and metastasis over unimodal counterpart, allowing accurate diagnosis and superior therapeutic outcomes.[215] To date, multifunctional HMNMs are highly praised for their widespread applications in image-guided cancer treatment.[28,63,86,216] Recently, silica shell coated Au/Gd nanoclusters (Au/GdNC@SiO$_2$) acted as a CT/MR dual-modal nanotracer for noninvasive labeling and tracking of transplanted human mesenchymal stem cells (hMSCs), without any adverse effect on functions including proliferation and differentiation of the labelled stem cells, even coupled with tracing the hMSCs transplanted in lungs for 7 days *via in vivo* CT/MR dual-modality imaging (Fig. 7A–C).[80]

Besides, PtCu$_3$ nanocages first performed as a HRP-like enzyme for catalytic decomposition of H$_2$O$_2$ in acidic media for CDT, and behaved as a GSH-POD mimic to promote GSH depletion *via* oxidation and further inhibited GSH-induced ROS scavenging in human umbilical vein endothelial cells and 4T1 cells. Furthermore, the dual-functional PtCu$_3$ nanocages worked as a sonosensitizer for cancer treatment guided by PA/CT dual-modal imaging under ultrasonication, together with minimal toxicity to normal tissues at therapeutic doses.[63] In addition, pH-responsive FePt-based NPs were reported as a treatment agent for real-time dual-modality MR/CT imaging both *in vivo* and *in vitro* to monitor tumour therapy.[86]

To make the therapy process more accurate, subtle integration of PTT with multiple imaging techniques is regarded as an encouraging strategy to achieve precise cancer therapy by acquiring more comprehensive and accurate information, certifying the feasibility to examine accumulated photothermal agents in tumors, assess size and location of tumors, monitor the PTT treatment process and evaluate treatment efficiency.[213,217] Accordingly, a large variety of theranostic HMNMs with multiple functions have been developed so far.[20,56,218]

Recently, Au–Fe$_2$C JNPs were developed and they showed an excellent photothermal effect due to their broad absorption in the NIR region.[56] By virtue of their superior magnetic and optical properties, Au–Fe$_2$C JNPs are demonstrated to be an ideal reagent for triple-modal MR/MSOT/CT imaging (Fig. 7D–G). Later on, Au$_3$Cu tetrapod nanocrystals (TPNCs) were synthesized and continuously functionalized with PEG, Cy5 and FA, termed as Au$_3$Cu@PEG–Cy5–FA. The resultant composite displayed high photostability, penetrability of deep tissue and desired PCE, finally exhibiting excellent MSOT in the NIR-II range and FL imaging potential towards selective treatment of tumors.[20]

Meanwhile, magnetic/plasmonic hybrid HMNMs are very promising for multi-modal imaging. To prove it, a ternary heteronanostructure (SeAuFe-EpC) was synthesized and specifically targeted to a tumor area, achieving multi-modal imaging-guided breast tumor RT (Fig. 7H–J).[188] The doped Se in SeAuFe-EpC NPs distinctly reduced the energy barrier, improved the electronic conductivity, facilitated the conversion of $^3O_2$ to singlet oxygen ($^1O_2$), induced irreversible death of tumor cells and ultimately realized a synergistic anti-cancer effect, as visibly identified by three-modality imaging of *in vivo* CT, PA and MR. Likewise, AgPt$_{alloy}$–Fe$_3$O$_4$ and Au$_{core}$@Pd$_{shell}$–Fe$_3$O$_4$ were designed with good hydrophilicity, making them ideal for MR imaging, PA imaging, CT imaging, and OCT in biomedical applications.[115]

As a feature of tumors, hypoxia has severe adverse effects on the outcomes of tumor chemotherapy, RT or PTT.[9,28,40,41] To conquer tumor hypoxia-induced RT tolerance, two-dimensional Pd@Au core–shell nanostructures (TPAN) were applied to stably produce O$_2$ for a long time by catalysis of endogenous H$_2$O$_2$, and their catalytic properties can be improved by surface plasmon resonance (SPR) effect.[40] By virtue of good photothermal efficiency and high NIR absorption, TPAN as a multi-modal imaging contrast gradually accumulated in tumor sites along with time variation due to enhanced permeability and retention (EPR) effect (Fig. 7K–M), as illustrated by X-ray, PA and NIR-II laser derived photothermal modality imaging, eventually achieving satisfactory therapeutic synergistic efficacy *in vivo* upon integration of radio and PTT. Overall, the above examples associated with precise cancer therapy are rational and feasible for promising clinic translation.

3.3 Therapy

Cancer is a group of diseases, and correlates to almost any part of human body, combined with inducing severe health problems and heavy social burdens.[219] In general, most clinicians still depend on conventional RT, chemotherapy and other surgery-mediated techniques for high-efficiency treatment of malignancies.[220] To date, many nanomaterial based therapeutic approaches have been developed for treatment of malignancies including PTT, PDT and CDT.[19,28,63,77] Among them, a series of HMNM-based studies have turned from single-therapy to subtly integrate the above techniques, as the advantages of synergistic therapy strategies are certified.[71,77,100,188,218] Notably, two types of lasers are usually used to visibly optimize PTT and PDT effects

in combined PTT/PDT, as well as suitable HMNMs with high PCE.[71,77]

3.3.1 Radiotherapy. RT can apply ionizing radiation to tumor sites by producing a vast number of free radicals (*e.g.* ROS) due to water radiolysis and/or other cellular components, leading to DNA damage and cell death.[187] Among conventional therapeutic techniques, RT plays a very important role in killing tumor cells by high-energy ionizing radiation in tumor theranostics.[221] So far, HMNMs have been developed as radiosensitizers for preclinical studies of cancer RT, as they can strongly absorb and deposit radiation.[40,187,188] Particularly, TPAN was used for transforming H_2O_2 to O_2, and its catalytic effect was significantly improved by the SPR effect initiated under laser irradiation to increase O_2 production and eliminate cancer hypoxia.[40] Also, a hollow PtCo nanosphere-based multifunctional radiosensitizer was facilely synthesized for RT enhancement, accompanied by showing dual efficient catalase-like activity and superior radiation absorption to cause more DNA damage, finally preventing tumor growth and relieving tumor hypoxia, as certified by *in vivo* and *in vitro* investigations.[222]

3.3.2 Chemotherapy. Currently, chemotherapy is the most common therapeutic in efficient management of patients with malignant tumors, and can adopt cytotoxic antineoplastic agents to induce direct cytotoxicity and thus eradicate tumor cells; however, its practical applications are limited because of severe side effects to normal tissues and undesirable therapeutic outcomes.[223] With rapid advance of nanotechnology, plenty of nanoplatforms have been established in cancer treatment, such as encapsulation of free drugs into HMNM-based nanomaterials, which effectively improved drug therapeutic efficiency and alleviated side effects mainly by specific uptake of the drugs in the targeted cancer cells.[29,59,224]

For example, porous Au@Pt NPs were constructed and they showed strong absorption in the NIR section and high PCE. After further functionalization with cRGD peptide and DOX, the nanocomposite exhibited observable reduction in OSD and seriously inhibited tumor growth by chemo-photothermal co-therapy, integrated with alleviation of DOX-induced oxidative damage.[29]

3.3.3 Photothermal therapy. Recently, tremendous progress has been made in cancer treatment.[225] However, conventional treatment modalities for cancer (*e.g.* surgery, chemotherapy and RT) are severely confined by high systemic toxicity and side effects.[226] Importantly, PTT is recognized as a noninvasive, temporal and spatial-controllable therapeutic modality for cancer treatment *via* hyperthermal tumor damage (*e.g.* protein denaturation and nucleic acid damnification), as well as little damage to normal tissues.[227] Notably, Au-based HMNMs have been explored in PTT, thanks to superior PCE performance upon NIR light irradiation and low cytotoxicity of Au.[20,56,66,97] This assumption is clearly evidenced by hollow Au NPs because of a larger surface area than solid counterparts.[66,228]

Lately, a Pt@Au nanoring@DNA (denoted as PAD for simplicity) probe was developed for FL imaging guided targeting PTT, and it behaved as an excellent photosensitizer upon NIR light irradiation in tumor cells, due to strong absorption of

Pt@Au nanorings.[66] The dual PAD probe holds great promise towards *in vitro* diagnosis and therapy of cancer cells (activated by NIR light such as the activation of specific recognition and FL imaging along with targeted PTT). Likewise, hybrid FePt/SiO$_2$/Au NPs were applied as a theranostic material for PTT and MR imaging of cancer urothelial (RT4) cells, by taking advantage of both magnetic and optical properties, which confirmed them as high efficiency and selective photo-thermal and MRI contrast agents, achieving highly selective and safe treatment of cancerous cells without any damage to healthy tissue.[97]

3.3.4 Photodynamic therapy. PDT is considered as a minimally-invasive and safe method for conventional cancer therapy, and provides treatment with little invasion and
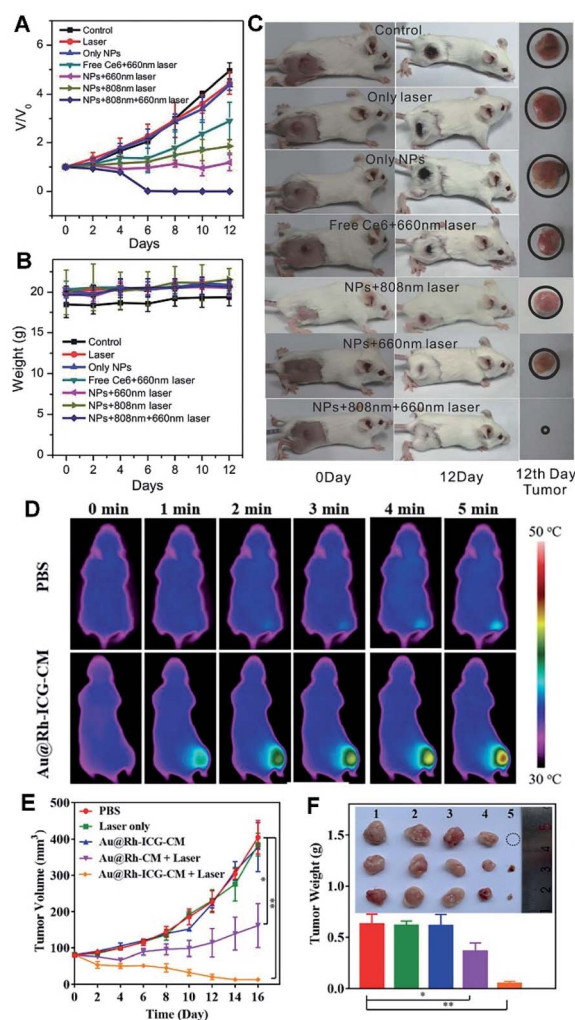

Fig. 8 (A) Changes in the tumor volumes of mice after different treatments. (B) Changes in the weights of mice in different groups. (C) Tumor changes of mice before and after treatment. Reproduced with permission.[41] Copyright 2018, Wiley. (D) Photothermal images of MDA-MB-231-tumor-bearing mice exposed to an 808 nm laser (0.3 W cm^{-2}) for 5 min. (E) Size changes of MDA-MB-231 tumors in nude mice under different treatments. (F) Average weights of tumors and photos of tumors harvested at 16 d from treatment of PBS: Laser only, Au@Rh−ICG−CM, Au@Rh-CM + Laser, and Au@Rh−ICG−CM + Laser (*$p < 0.05$, **$p < 0.01$). Reproduced with permission.[28] Copyright 2018, Wiley.

negligible drug resistance and side effects.[229] In a photodynamic system, light irradiation is precisely centered on the target tumor tissue, where the excited photosensitizer interacts with adjacent molecules to generate ROS or localized heating.[230] Simply speaking, ROS are free radicals and highly reactive ions, which can cause severe oxidative damage to tumor tissues and induce *in situ* irreversible destruction, thereby effectively eliminating cancer cells.[231]

For example, biomimetic MnO_2@PtCo nanoflowers were fabricated with catalase-like and oxidase-like properties, which effectively relieved hypoxic conditions and simultaneously induced cell death *via* the ROS-mediated mechanism, showing significant improvement in tumor therapy.[82] Similarly, a bimetallic AuPt nanozyme was synthesized with help of silk fibroin, which effectively transformed adsorbed O_2 and endogenous H_2O_2 into $\cdot O_2^-$ and $\cdot OH$, respectively,[216] finally inducing irreversible damage to tumor cells in tumor-bearing mice.

To increase the PDT efficacy, a photosensitizer-Pd@Pt nanoplates with catalase-like activity was developed by subsequent immobilization of PEG and Ce6 (termed Pd@Pt–PEG–Ce6), which delivered Ce6 to the cancer cells and efficiently converted H_2O_2 into O_2 for the Pd@Pt based theranostic nanosystem, hence remarkably increasing the efficacy of PDT (Fig. 8A–C).[41] In another example, a nanoplatform was built by loading ICG in cavity of porous Au@Rh–CM (Au@Rh–ICG–CM), which exhibited high-quality FL and PA imaging effects, in turn revealing extremely efficient PDT efficacy in tumor treatment (Fig. 8D–F).[28] The successful examples not only facilitate advance of HMNMs in hypoxic tumor theranostics, but also offer some valuable guidelines for establishing other nanosystems in cancer therapy.

3.3.5 Chemodynamic therapy. CDT mainly depends on *in situ* Fenton or Fenton-like reactions by producing a vast amount of ROS by photosensitizers upon exposure to UV-vis-NIR light for ablating cancer cells.[232,233] Impressively, photothermal agents can greatly accelerate Fenton-like reactions by elevating the local temperature or reducing the local pH value of the tumor, ultimately converting optical energy into hyperthermia, as widely adopted in recent literature.[29,100,211,224,234] For example, Cu_2Se hollow nanocubes (HNCs) were prepared with high PCE and improved Fenton-like properties.[44] After surface modification with PEG, the hybrid PEG-Cu_2Se HNCs displayed photothermal-enhanced CDT, achieving significantly enhanced efficacy in 4T1 tumor bearing mice (Fig. 9A–C).
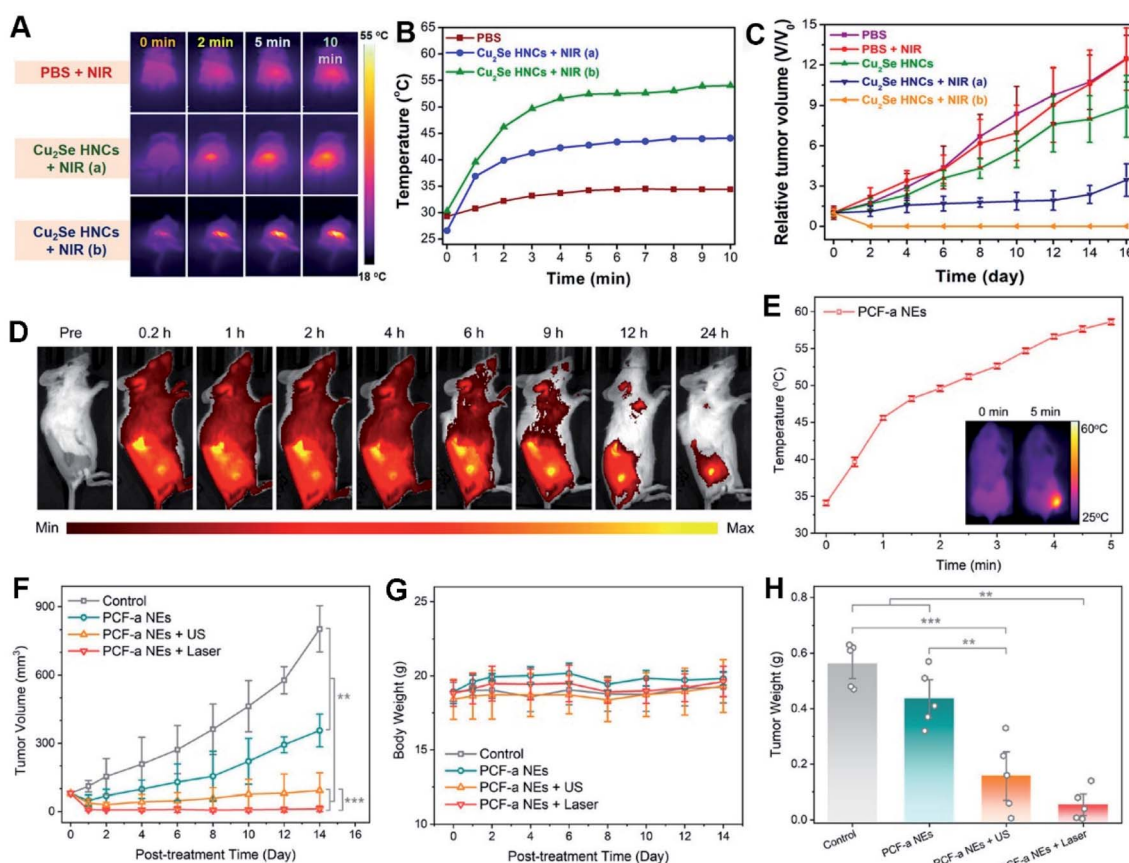

Fig. 9 *In vivo* photothermal-enhanced CDT with PEG-Cu_2Se HNCs. (A) IR thermal images and (B) temperature changes at the tumor sites of 4T1 tumor-bearing mice. (C) Relative tumor growth curves. Reproduced with permission.[44] Copyright 2018, Wiley. (D) Fluorescence imaging of 4T1 tumor-bearing mice after intravenous injection of Cy5.5-labeled PCF-a NEs. (E) Temperature growth curve of the tumor site with PCF-a NEs under 808 nm laser irradiation. The inset shows the infrared thermal images. (F) Tumor growth curves. (G) Average body weights of mice. (H) Average weights of tumors (*$p < 0.05$, **$p < 0.01$, and ***$p < 0.001$). Reproduced with permission.[21] Copyright 2021, American Chemical Society.

As known, US can create highly concentrated shock waves by intense local vibration and yield more ROS due to acoustic cavitation effect, accompanied by boosting mass transfer of a nanozyme, in turn significantly accelerating a Fenton or Fenton-like reaction for CDT.[21,232] Thereby, subtle integration of US with CDT onto the nanozyme can effectively prevent tumor growth and recurrence.[21,235,236] For example, ultra-small PdCuFe alloy nanozymes (PCF-a NEs) were developed, which showed high PCE and competent GSH-Px-like and POD-like activity in circumneutral pH for highly enhanced synergistic CDT and PTT treatment within the NIR scope, exemplifying the high-efficiency tumor inhibition by the as-built artificial enzyme (Fig. 9D–H).[21]

The above examples demonstrate feasibility of utilizing HMNM-based nanozymes for highly specific tumor therapy enhanced by external stimuli, and then illustrate the correlations of respective compositions and structures with the properties of such nanozymes.

3.3.6 Synergistic therapy. Recent studies have shifted from individual to synergistic therapy by subtly combining different therapy techniques (*e.g.* PTT, PDT and CDT) for comprehensive diagnosis and high-efficiency treatment of cancers.[237] To date, a variety of synergistic research studies associated with multifunctional HMNM nanoplatforms demonstrate significantly improved treatment of malignancies and minimized side effects based on integrated multiple modalities.[32,71,77,206] For

instance, a multifunctional star-like Au/Pt nanosystem was established by sequential GSH-triggered catalysis for tumor imaging and eradication, showing high specificity to tumor sites through FA during *in vivo* experiments.[32] By triggering with GSH, the S–S was broken, followed by release of IR780 for PTT&PDT and imaging with assistance of the Pt nanolayer in the Au/Pt stars and GOx in sequential catalytic system (Fig. 10A). Importantly, GOx showed high catalytic behavior towards endogenous glucose to generate H_2O_2 and sequentially convert H_2O_2 to $^{\bullet}OH$ by taking the POD-like property of the Pt layer.

Likewise, Au eyeball-like yolk–shell Au@Pd NPs were prepared with open-mouthed Pd shells and then immobilized with FA and Ce6, which displayed excellent photodynamic efficacy of Ce6 upon irradiation and high specificity of conjugated FA to target MCF-7 cancer cells in broad NIR window, eventually harvesting synergistic PDT&PTT inducing cell apoptosis.[71]

Although synergistic therapy demonstrates great promise for highly efficient cancer treatment, it is still a huge challenge to build a multi-functional nanosystem by a simple and high-efficiency strategy. For example, Au_2Pt NPs with multiple functions were facilely synthesized at room temperature, followed by successive covalent linkage of SH–PEG–NH_2 and Ce6 to transform O_2 to $^1O_2$, and they exhibited catalase-like ability to convert H_2O_2 to O_2 for relaxation of tumor hypoxia and improvement in PDT efficiency, combined with the POD-like activity to produce
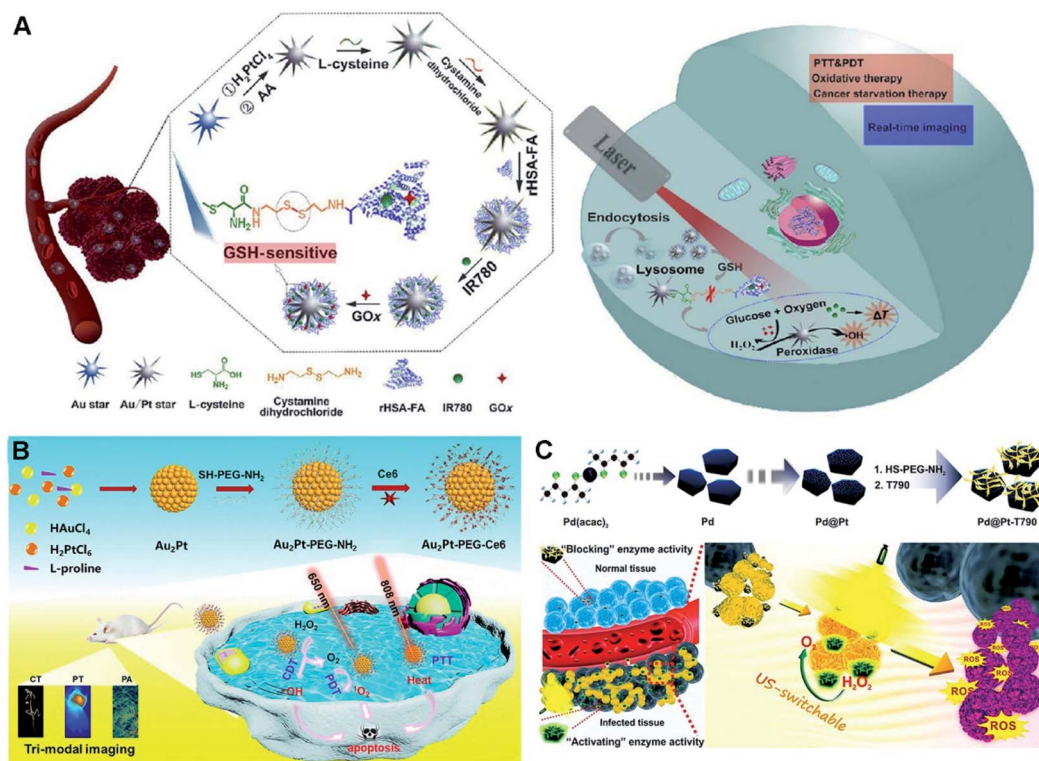

Fig. 10 (A) Schematic diagram of the synthesis process and multifunctional application *in vivo* of the probes. Reproduced with permission.[32] Copyright 2020, Springer. (B) Schematic diagram of the preparation of Au_2Pt-PEG-Ce6 and multi-modal imaging-guided synergistic PTT/PDT/CDT. Reproduced with permission.[218] Copyright 2020, Elsevier. (C) Schematic illustration of the synthesis process of the Pd@Pt-T790 nanoplatform and its US-switchable nanozyme catalytic enhanced SDT for bacterial infection. Reproduced with permission.[33] Copyright 2020, American Chemical Society.

˙OH for CDT (Fig. 10B).[218] Furthermore, the Au$_2$Pt-PEG-Ce6 with dual enzyme-like properties provided possibility of PA and photothermal guided NIR-responsive PTT as a photothermal transition agent, owing to high PCE in the NIR region. In addition, the Au$_2$Pt-PEG-Ce6 nanoformulation acted as a contrast agent for CT imaging. Overall, the multifunctional platform presented great potential in multimodal imaging-guided synergistic PTT/PDT/CDT with remarkable tumor specificity and enhanced therapy of tumors.

To date, NIR laser-mediated PTT has received tremendous attention as a non-invasive therapy to directly kill tumor cells and improve the tumor hypoxic microenvironment, where many HMNMs have been applied as high-efficiency photothermal agents in the PTT of cancers.[66,97] However, such agents hardly completely ablate tumors, particularly deep-seated cancers, owing to insufficient absorption efficiency of natural tissue absorbents.[9,26] For effective cancer theranostics, several examples confirm effectiveness of combining PTT with other therapeutic techniques such as RT in a single platform.[9,26]

Quan et al. reported Cys-coated FePd nanodots with a high absorption located at 1064 nm, which produced effective hyperthermia (35.4%) with an improved radiation effect, combined by working as a contrast agent for CT/MR/PA

imaging.[9] Besides, PEGylated Au@Pt nanodendrites were constructed as an improved theranostic agent for sharply enhanced synergistic PTT/RT therapy and CT imaging in the NIR scope relative to single RT or PTT.[26] As a result, the integration of Au@Pt nanodendrites improved RT with PTT, and more effectively suppressed the growth of cancer cells in this research.

However, the limited penetration depth severely restricts their extensive PDT application, especially in deeply located cancers.[33] Fortunately, recently emerged SDT, as a type of ROS-based noninvasive therapeutic modality, shows effective treatment of deep-seated tumors triggered by US.[63,238] For example, an US-switchable nanozyme is desirable to strengthen SDT against deep-seated bacterial infection by producing catalytic oxygen (Fig. 10C).[33] As shown, a hybrid nanoplatform was built by modifying Pd@Pt nanoplates with organic sonosensitizer T790 (Pd@Pt-T790). Such a modification severely inhibited the catalase-like activity of the as-formed nanoenzyme, which was recovered upon US irradiation. By virtue of this US-switchable enzyme, the Pd@Pt-T790-based nanotherapeutic bioplatform completely eradicated the myositis caused by MRSA in vitro and in vivo upon US irradiation, accompanied by supervising the SDT progress through PA and MR imaging.
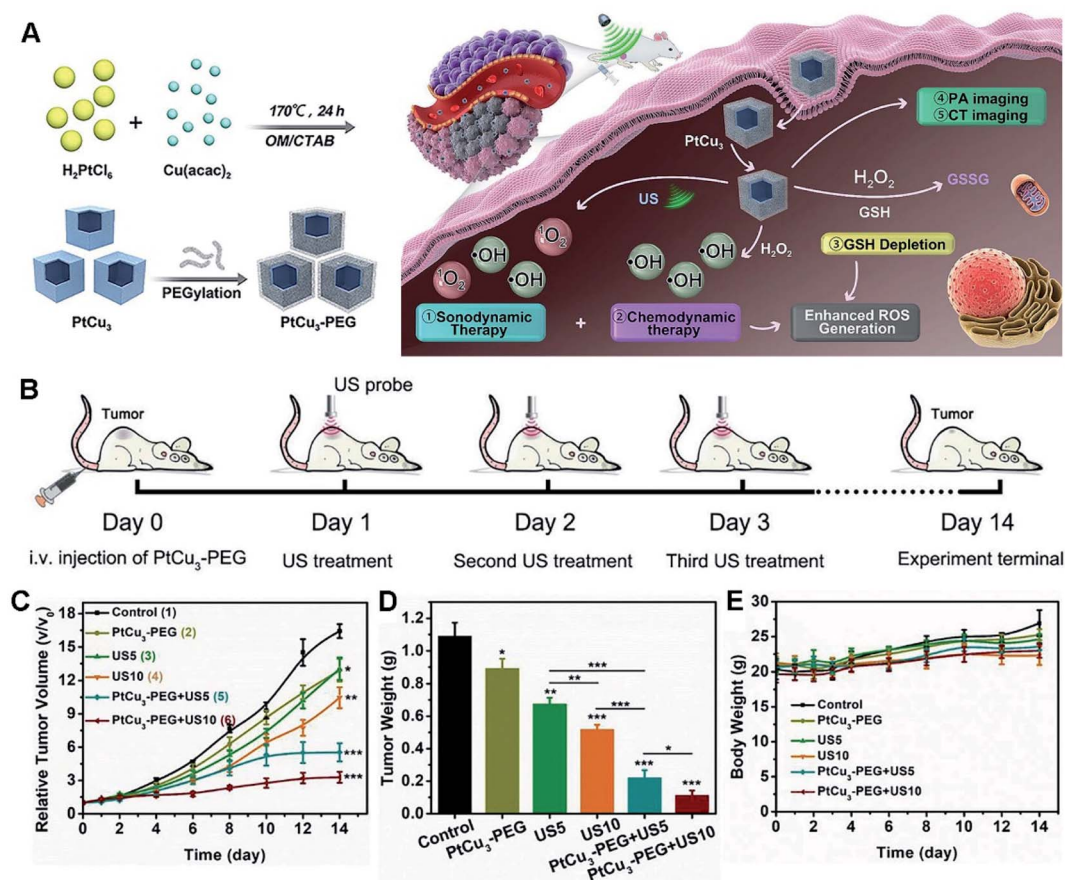

Fig. 11 (A) Schematic illustration of PA/CT dual-modal imaging guided cancer CDT and GSH depletion enhanced SDT by PtCu$_3$ nanocages. (B) Schematic diagram of the treatment process for SDT mediated by PtCu$_3$-PEG in a 4T1 tumor model. (C) Tumor growth curves of mice treated with different ways. (D) Tumor weights at the end ($*p < 0.05$, $**p < 0.01$, $***p < 0.001$). (E) Body weight changes during the treatment. Reproduced with permission.[63] Copyright 2019, Wiley.

Also, CDT appears as another kind of ROS-derived therapeutic technique for effective treatment of deep-seated tumors, by subtly exploiting two characteristics, namely acidity and overexpressed H_2O_2 in internal complicated tumor microenvironment without any external stimulus.[63] To improve the effect of CDT-enhanced SDT, $PtCu_3$ nanocages were developed as a sonosensitizer to yield ROS under US irradiation in 4T1-bearing mice (Fig. 11).[63] Importantly, $PtCu_3$ nanocages functioned as a HRP-like nanozyme to catalyze H_2O_2 by forming $\cdot OH$ for CDT, and simultaneously worked as a GSH-Px like enzyme to accelerate GSH depletion, thus weakening the ability of GSH to eliminate ROS. More importantly, the $PtCu_3$ cages have the capacity to realize effective CDT-enhanced SDT *via* GSH elimination, along with PA/CT multi-modal imaging of tumor-bearing mice.

3.4 Others

3.4.1 Antioxidation. Currently, most studies have focused on individual Ag and Au NPs due to their good conductivity and strong antioxidation ability.[239,240] Nevertheless, they are hardly explored alone in practice, due to scarcity of Au and weak resistance of Ag NPs to ion transport.[241] Therefore, HMNM-based candidates have been synthesized owing to their cost-effectiveness, competent conductivity and strong durability towards ion transfer in biomedical field.[242,243] Thus, a large

number of HMNM-based nanozymes have been prepared as antioxidants to scavenge ROS.[29,244]

For instance, a triM nanozyme was developed with high multiple catalytic activities and environmental selectivity, showing significant preference for effective elimination of ROS and reactive nitrogen species (RNS) in neutral media (Fig. 12).[244] As shown by *in vitro* experiments, the triM nanozyme clearly boosted viability of destructed nerve cells. Meanwhile, lipid peroxidation and superoxide dismutase (SOD) activity were greatly recovered upon treatment with the triM nanozyme in an *in vivo* test.

3.4.2 Antibacteria. Bacterial infections are some of the main factors of death in clinics, particularly with the emergence of multidrug resistant (MDR) bacteria, and it is critical yet challenging to kill them only with antibiotics in most cases.[245,246] In order to replace antibiotics, many nanomaterials such as MMNMs (*e.g.* Ag, Au and Cu) exhibit appealing antibacterial ability and improved antibacterial efficacy as well as negligible cytotoxicity for effective treatment of infectious diseases in a broad spectrum range, as unveiled by recent studies, due to their superior properties to routine antibiotics conventionally employed.[18]

Among them, Ag NPs have been extensively investigated due to their high antibacterial efficacy.[18,245] However, their poor stability and serious cytotoxicity for mammalian cells seriously
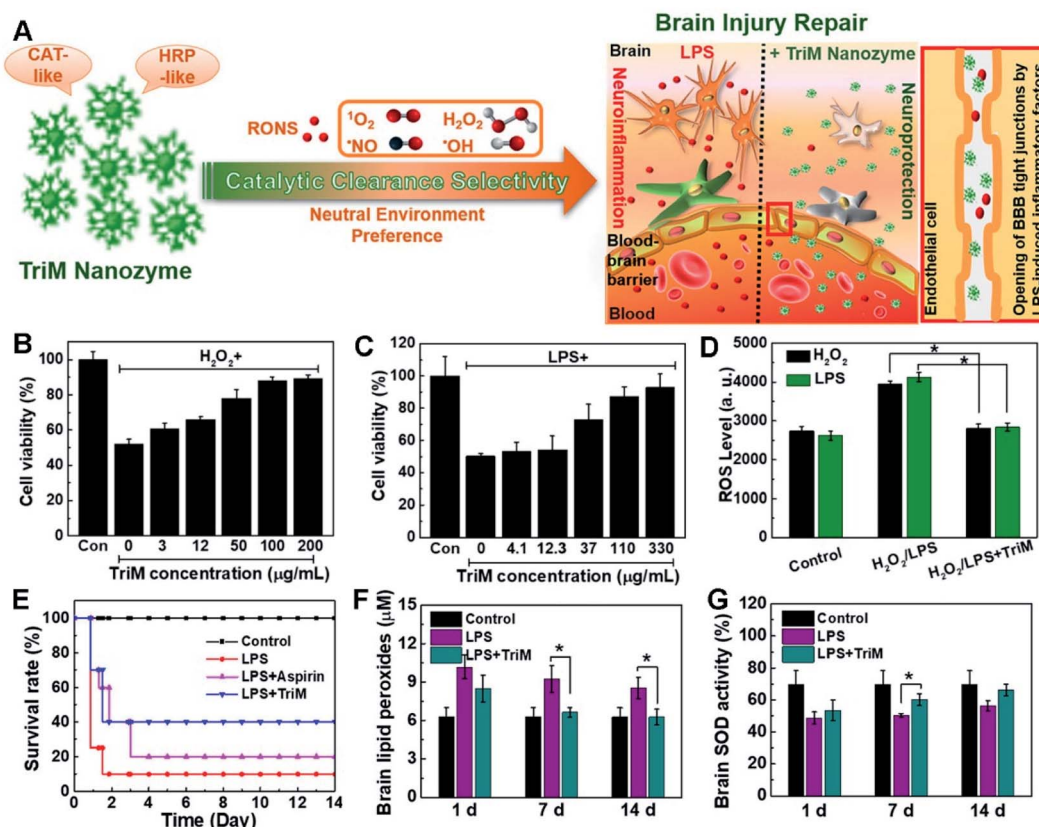

Fig. 12 (A) Schematic illustration of the brain injury repair mechanism of the triM nanozyme. Cell viability of (B) H_2O_2– or (C) LPS–treated N2a cells in the presence of trim nanozymes. (D) Quantitative analyses of ROS levels with the triM nanozyme treatment in H_2O_2– or LPS–stimulated N2a cells. (E) Survival curves of mice with or without treatment of triM nanozymes. (F) Lipid peroxides and (G) SOD activity assays in the brain. Reproduced with permission.[244] Copyright 2019, American Chemical Society.

confine their further applications.[247] To overcome the present bottlenecks, HMNMs are regarded as good alternatives owing to the superior bio-compatibility and antibacterial properties, making them suitable for therapeutic applications.[27,34,189,247] Importantly, carbohydrate-coated Au–Ag NPs were minimally toxic to mammalian cells, but showed more toxicity to MDR *Enterobacter cloacae* and *Escherichia coli* than most potent antibiotics.[247] Interesting, *in vivo* results showed enhanced efficiency of elimination of MDR MRSA in mice skin wounds by Au–Ag NPs compared to gentamicin, eventually promoting fast healing of the infected wounds.

Similarly, Ag$^+$ ions were efficiently released by oxidative etching from the external Ag shell in Au/Ag NRs, which were *in situ* noninvasively monitored by PA imaging.[27] Moreover, the hybrid particles showed strong bactericidal efficacy by killing over 99.99% of both methicillin-resistant MRSA (32 μM Ag$^+$ equivalent) and *Escherichia coli* (8 μM Ag$^+$ equivalent) for high-efficiency coalescence of MRSA skin infections. These nanosystems provide promising tools with on-demand antimicrobial and self-reporting abilities for imaging and therapy of infectious diseases *in vivo*.
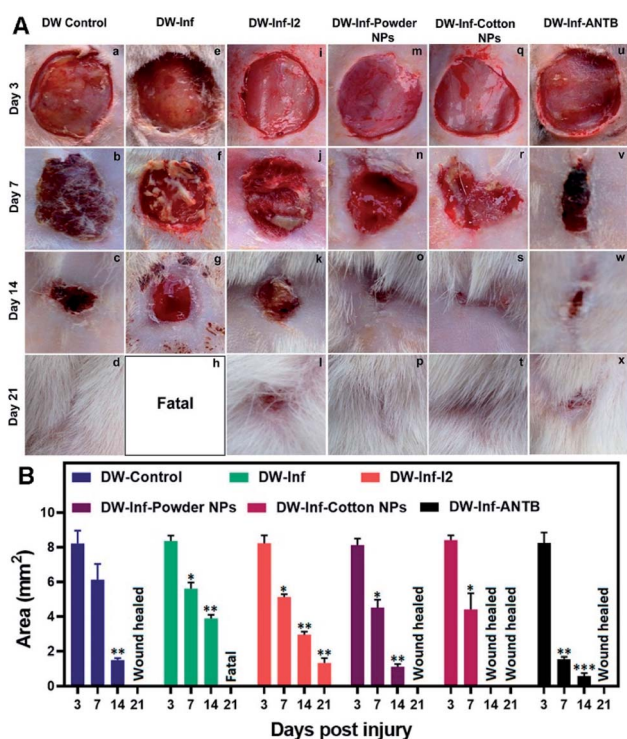

Fig. 13 (A) Photographs representing the *in vivo* study on the effects of treatment with the prepared wound healing materials on MRSA infection-induced DW in rats. (a–d) Untreated simple DW. (e–h) Untreated infected DW. (i–l) Infected DW treated with iodine. (m–p) Infected DW treated with the powder nanocomposite. (q–t) Infected DW treated with a nanocomposite impregnated cotton swab. (u–x) Infected DW treated with a topical antibiotic. (B) Results of wound area measurement done at 3, 7, 14, and 21 days after infliction of injury. Reproduced with permission.[248] Copyright 2019, American Chemical Society.

Beyond the above, Fe–Cu NPs were prepared and subsequently impregnated onto cotton cloth, which showed strong antimicrobial activity for MDR MRSA, Gram positive/negative bacteria, and fungus in humans, coupled with good biocompatibility and broad-spectrum antimicrobial properties.[248] Importantly, the hybrid composite displayed good wound healing ability by inhibiting microbial growth of several types of microbes and found feasibility for treatment of Wistar albino rats with infected diabetic wounds (DW), as evidenced by *in vivo* tests (Fig. 13).

4. Conclusions and prospects

In summary, HMNMs and derived nanomaterials show high improvement in physicochemical properties by finely modulating microstructural parameters (*e.g.* size, shape, composition, structure, and surface modification) to regulate the spatial arrangement patterns and local electronic structures in scalable synthesis, combined with exploring their potential applications in clinical practice, as supported by the collected research. The attractive activities of HMNMs endow them with wider biomedical applications than that of MMNMs in the above summaries, which is mainly attributed to the aforementioned synergistic effects between different metals.

Although substantial developments have been already made in the aforementioned HMNMs (frequently prepared by trial-and-error methods), their theoretical design and controllable synthesis even at the atomic level are always required for building reliable clinical devices to overcome new issues emerging in practice. Besides, the long-term biological safety, large-scale production, quality control, and insufficient knowledge related to pharmacokinetics are still issues in potential biomedical applications. Further, theoretical studies based on density functional theory are urgent yet challenging to have in-depth cognition of the interfacial interactions between HMNMs and biomolecules. There is no doubt that the era of controlled synthesis and biomedical applications of HMNMs is coming.

Author contributions

Shan–Shan Li: investigation, methodology, writing – original draft, funding acquisition. Ai-Jun Wang: investigation, methodology. Pei-Xin Yuan, Li-Ping Mei, and Lu Zhang: investigation. Jiu-Ju Feng: writing – original draft, writing – review & editing.

Conflicts of interest

There are no conflicts to declare.

Abbreviations

HMNMs	Heterometallic nanomaterials
MMNMs	Monometallic nanomaterials
NPs	Nanoparticles
TPNCs	Tetrapod nanocrystals

PTT	Photothermal therapy		GO	Graphene oxide
NIR	Near-infrared		C3N4	Graphitic carbon nitride
NIR-II	Second near-infrared		GQDs	Nitrogen-doped graphene quantum dots
CDT	Chemodynamic therapy		OMC	Ordered mesoporous carbon
BNCs	Bimetallic nanoclusters		HAC	High-active carbon
ECL	Electrochemiluminescence		CB	Carbon black
CA	Carbohydrate antigen		GDY	Graphdiyne
BSA	Bovine serum albumin		SWCNT	Single-walled carbon nanotube
rBSA	Reduced bovine serum albumin		Thi	Thionine
CT	Computed tomography		MSNs	Mesoporous silica nanoparticles
PA	Photoacoustic		MR	Magnetic resonance
T790	*meso*-Tetra(4-carboxyphenyl)porphine		ctDNA	Circulating tumor DNA
US	Ultrasound		hMSCs	Human mesenchymal stem cells
SDT	Sonodynamic therapy		IgG	Immunoglobulin G
MRSA	Methicillin-resistant *Staphylococcus aureus*		NSE	Neuron-specific enolase
TPAN	Two-dimensional Pd@Au core–shell nanostructure		SCCA	Squamous cell carcinoma antigen
			CYSC	Cystatin C
SPR	Surface plasmon resonance		PEC	Photoelectrochemical
RT	Radiotherapy		ALP	Alkaline phosphatase
HNCs	Hollow nanocubes		PCN-223-Fe	Iron-porphyrinic metal–organic framework
PCE	Photothermal conversion efficiency			
PCF-a NEs	PdCuFe alloy nanozymes		PRL	Prolactin
POD	Peroxidase		LAG-3	Lymphocyte activation gene-3
cTnI	Cardiac troponin I		TMB	3,3′,5,5′-Tetramethylbenzidine
JNPs	Janus nanoparticles		CFP-10	Anticulture filtrate protein-10
SERS	Surface enhanced Raman scattering		CK-MB	Creatine kinase-MB
OTA	Ochratoxin A		HE4	Human epididymis protein 4
TEM	Transmission electron microscope		HER2	Human epidermal growth factor receptor 2
HR-TEM	High-resolution TEM		NT-proBNP	N-Terminal pro-B-type natriuretic peptide
HAADF	High-angle annular dark field		PCT	Procalcitonin
STEM	Scanning transmission electron microscope		SARS-CoV-2	Severe acute respiratory syndrome coronavirus 2
SEM	Scanning electron microscope			
CM	Cell membrane		miRNAs	MicroRNAs
DOX	Doxorubicin		LOD	Limit of detection
OSD	Oxidative stress damage		FL	Fluorescence
2D	Two-dimensional		LSPR	Localized surface plasmon resonance
3D	Three-dimensional		SPR	Surface plasmon resonance
ROS	Reactive oxygen species		2PPL	Two-photon photoluminescence
GOx	Glucose oxidase		AFM	Atomic force microscopy
HTNs	Hollow nanotriangles		uPA	Urokinase-type plasminogen activator
PAD	Pt@Au nanoring@DNA		MMP	Matrix metalloproteinase
SH-PEG	Thiolated polyethylene glycol		5-TAMRA	5-Aminomethyl Rhodamine
HRP	Horseradish peroxidase		FITC	Fluorescein isothiocyanate
GSH-Px	Glutathione peroxidase		LPS	Lipopolysaccharide
FA	Folic acid		TPP	Triphenylphosphine
Ce6	Chlorin e6		4-TPA	4-Thiophenylacetylene
MSOT	Multispectral photoacoustic tomography		ssDNA	Single-stranded DNA
4-MBA	4-Mercaptobenzoicacid		PEB	3-[4-(Phenylethynyl)benzylthio]propanoic acid
dsDNA	Double-stranded DNA		PEITC	2-Phenethyl isothiocyanate
CTCs	Circulating tumor cells		$Cu_3(BTC)_2$	Copper(ɪɪ) carboxylate MOFs
GSH	Glutathione		ICG	Indocyanine green
Cys	Cysteine		OCT	Optical coherence tomography
PBS	Phosphate buffer solution		EPR	Enhanced permeability and retention
PDT	Photodynamic therapy		RNS	Reactive nitrogen species
MOFs	Metal organic frameworks		triM	Trimetallic
CEA	Carcinoembryonic antigen		SOD	Superoxide dismutase
PSA	Prostate antigen		MDR	Multidrug resistant
AFP	Alpha fetoprotein		DW	Diabetic wounds
rGO	Reduced graphene oxide			

Acknowledgements

Notes and references

1 C. Gao, F. Lyu and Y. Yin, *Chem. Rev.*, 2021, **121**, 834–881.

2 U. B. Kim, D. J. Jung, H. J. Jeon, K. Rathwell and S.-g. Lee, *Chem. Rev.*, 2020, **120**, 13382–13433.

3 Y. Liu, J. Li, M. Chen, X. Chen and N. Zheng, *Theranostics*, 2020, **10**, 10057–10074.

4 Z. Fan and H. Zhang, *Chem. Soc. Rev.*, 2016, **45**, 63–82.

5 K. D. Gilroy, A. Ruditskiy, H.-C. Peng, D. Qin and Y. Xia, *Chem. Rev.*, 2016, **116**, 10414–10472.

6 C.-L. Yang, L.-N. Wang, P. Yin, J. Liu, M.-X. Chen, Q.-Q. Yan, Z.-S. Wang, S.-L. Xu, S.-Q. Chu, C. Cui, H. Ju, J. Zhu, Y. Lin, J. Shui and H.-W. Liang, *Science*, 2021, **374**, 459–464.

7 M. Zhou, C. Li and J. Fang, *Chem. Rev.*, 2021, **121**, 736–795.

8 Y. Wang, L. Cao, N. J. Libretto, X. Li, C. Li, Y. Wan, C. He, J. Lee, J. Gregg, H. Zong, D. Su, J. T. Miller, T. Mueller and C. Wang, *J. Am. Chem. Soc.*, 2019, **141**, 16635–16642.

9 M. Lyu, D. Zhu, Y. Duo, Y. Li and H. Quan, *Biomaterials*, 2020, **233**, 119656.

10 L. Wang, A. Holewinski and C. Wang, *ACS Catal.*, 2018, **8**, 9388–9398.

11 M. Wang, L. Wang, H. Li, W. Du, M. U. Khan, S. Zhao, C. Ma, Z. Li and J. Zeng, *J. Am. Chem. Soc.*, 2015, **137**, 14027–14030.

12 K. Loza, M. Heggen and M. Epple, *Adv. Funct. Mater.*, 2020, **30**, 1909260.

13 M. Zhao, Z. D. Hood, M. Vara, K. D. Gilroy, M. Chi and Y. Xia, *ACS Nano*, 2019, **13**, 7241–7251.

14 Z. Lyu, S. Zhu, L. Xu, Z. Chen, Y. Zhang, M. Xie, T. Li, S. Zhou, J. Liu, M. Chi, M. Shao, M. Mavrikakis and Y. Xia, *J. Am. Chem. Soc.*, 2021, **143**, 149–162.

15 W. Niu, Y. A. A. Chua, W. Zhang, H. Huang and X. Lu, *J. Am. Chem. Soc.*, 2015, **137**, 10460–10463.

16 D. Zhang, B. Gökce and S. Barcikowski, *Chem. Rev.*, 2017, **117**, 3990–4103.

17 B. Unnikrishnan, C.-W. Lien, H.-W. Chu and C.-C. Huang, *J. Hazard. Mater.*, 2021, **401**, 123397.

18 P. Makvandi, C.-y. Wang, E. N. Zare, A. Borzacchiello, L.-n. Niu and F. R. Tay, *Adv. Funct. Mater.*, 2020, **30**, 1910021.

19 F. He, H. Ji, L. Feng, Z. Wang, Q. Sun, C. Zhong, D. Yang, S. Gai, P. Yang and J. Lin, *Biomaterials*, 2021, **264**, 120453.

20 Z. Wang, Y. Ju, S. Tong, H. Zhang, J. Lin, B. Wang and Y. Hou, *Nanoscale Horiz.*, 2018, **3**, 624–631.

21 D. Jana, D. Wang, A. K. Bindra, Y. Guo, J. Liu and Y. Zhao, *ACS Nano*, 2021, **15**, 7774–7782.

22 L. Zhang, L. T. Roling, X. Wang, M. Vara, M. Chi, J. Liu, S.-I. Choi, J. Park, J. A. Herron, Z. Xie, M. Mavrikakis and Y. Xia, *Science*, 2015, **349**, 412.

23 M. Chen, J. P. Liu and S. Sun, *J. Am. Chem. Soc.*, 2004, **126**, 8394–8395.

24 L. Fu, X. Gao, S. Dong, H.-Y. Hsu and G. Zou, *Anal. Chem.*, 2021, **93**, 4909–4915.

25 Z. Chu, L. Chen, X. Wang, Q. Yang, Q. Zhao, C. Huang, Y. Huang, D.-P. Yang and N. Jia, *ACS Biomater. Sci. Eng.*, 2019, **5**, 1005–1015.

26 X. Liu, X. Zhang, M. Zhu, G. Lin, J. Liu, Z. Zhou, X. Tian and Y. Pan, *ACS Appl. Mater. Interfaces*, 2017, **9**, 279–285.

27 T. Kim, Q. Zhang, J. Li, L. Zhang and J. V. Jokerst, *ACS Nano*, 2018, **12**, 5615–5625.

28 J. Wang, J. Sun, W. Hu, Y. Wang, T. Chou, B. Zhang, Q. Zhang, L. Ren and H. Wang, *Adv. Mater.*, 2020, **32**, 2001862.

29 Q. Yang, J. Peng, Y. Xiao, W. Li, L. Tan, X. Xu and Z. Qian, *ACS Appl. Mater. Interfaces*, 2018, **10**, 150–164.

30 Y. Jia, Y. Li, S. Zhang, P. Wang, Q. Liu and Y. Dong, *Biosens. Bioelectron.*, 2020, **149**, 111842.

31 W. Fang, Z. Cheng, Y. Yang, A. Shen and J. Hu, *Appl. Mater. Today*, 2019, **15**, 252–262.

32 A. Zhang, Q. Zhang, G. Alfranca, S. Pan, Z. Huang, J. Cheng, Q. Ma, J. Song, Y. Pan, J. Ni, L. Ma and D. Cui, *Nano Res.*, 2020, **13**, 160–172.

33 D. Sun, X. Pang, Y. Cheng, J. Ming, S. Xiang, C. Zhang, P. Lv, C. Chu, X. Chen, G. Liu and N. Zheng, *ACS Nano*, 2020, **14**, 2063–2076.

34 Y. Peng, Y. Liu, X. Lu, S. Wang, M. Chen, W. Huang, Z. Wu, G. Lu and L. Nie, *J. Mater. Chem. B*, 2018, **6**, 2813–2820.

35 L. Fan, Y. Yan, B. Guo, M. Zhao, J. Li, X. Bian, H. Wu, W. Cheng and S. Ding, *Sens. Actuators, B*, 2019, **296**, 126697.

36 X.-Y. Ge, Y.-G. Feng, S.-Y. Cen, A.-J. Wang, L.-P. Mei, X. Luo and J.-J. Feng, *Anal. Chim. Acta*, 2021, **1176**, 338750.

37 P. Song, L.-L. He, A.-J. Wang, L.-P. Mei, S.-X. Zhong, J.-R. Chen and J.-J. Feng, *J. Mater. Chem. A*, 2015, **3**, 5321–5327.

38 S.-S. Li, A.-J. Wang, Y.-Y. Hu, K.-M. Fang, J.-R. Chen and J.-J. Feng, *J. Mater. Chem. A*, 2014, **2**, 18177–18183.

39 S.-S. Li, J.-J. Lv, Y.-Y. Hu, J.-N. Zheng, J.-R. Chen, A.-J. Wang and J.-J. Feng, *J. Power Sources*, 2014, **247**, 213–218.

40 Y. Yang, M. Chen, B. Wang, P. Wang, Y. Liu, Y. Zhao, K. Li, G. Song, X.-B. Zhang and W. Tan, *Angew. Chem., Int. Ed.*, 2019, **58**, 15069–15075.

41 J. Wei, J. Li, D. Sun, Q. Li, J. Ma, X. Chen, X. Zhu and N. Zheng, *Adv. Funct. Mater.*, 2018, **28**, 1706310.

42 Y. Shi, Z. Lyu, M. Zhao, R. Chen, Q. N. Nguyen and Y. Xia, *Chem. Rev.*, 2021, **121**, 649–735.

43 T.-H. Yang, J. Ahn, S. Shi, P. Wang, R. Gao and D. Qin, *Chem. Rev.*, 2021, **121**, 796–833.

44 X. Wang, X. Zhong, H. Lei, Y. Geng, Q. Zhao, F. Gong, Z. Yang, Z. Dong, Z. Liu and L. Cheng, *Chem. Mater.*, 2019, **31**, 6174–6186.

45 Z.-P. Wu, S. Shan, S.-Q. Zang and C.-J. Zhong, *Acc. Chem. Res.*, 2020, **53**, 2913–2924.

46 X.-Y. Wang, Y. Chen, L.-P. Mei, A.-J. Wang, P.-X. Yuan and J.-J. Feng, *Sens. Actuators, B*, 2020, **315**, 128088.

47 Y. Chen, L.-P. Mei, J.-J. Feng, P.-X. Yuan, X. Luo and A.-J. Wang, *Biosens. Bioelectron.*, 2019, **145**, 111638.

48 A. J. McGrath, Y.-H. Chien, S. Cheong, D. A. J. Herman, J. Watt, A. M. Henning, L. Gloag, C.-S. Yeh and R. D. Tilley, *ACS Nano*, 2015, **9**, 12283–12291.

49 X.-Y. Wang, Y.-G. Feng, A.-J. Wang, L.-P. Mei, P.-X. Yuan, X. Luo and J.-J. Feng, *Sens. Actuators, B*, 2021, **331**, 129460.

50 S.-Y. Cen, Y.-G. Feng, J.-H. Zhu, X.-Y. Wang, A.-J. Wang, X. Luo and J.-J. Feng, *Sens. Actuators, B*, 2021, **333**, 129573.

51 Y. Chen, X.-Y. Wang, A.-J. Wang, L.-P. Mei, P.-X. Yuan, X. Luo and J.-J. Feng, *Sens. Actuators, B*, 2021, **326**, 128794.

52 Y. Chen, A.-J. Wang, P.-X. Yuan, X. Luo, Y. Xue and J.-J. Feng, *Biosens. Bioelectron.*, 2019, **132**, 294–301.

53 G. Loget, D. Zigah, L. Bouffier, N. Sojic and A. Kuhn, *Acc. Chem. Res.*, 2013, **46**, 2513–2523.

54 X. Zhang, Q. Fu, H. Duan, J. Song and H. Yang, *ACS Nano*, 2021, **15**, 6147–6191.

55 M.-J. Zhu, J.-B. Pan, Z.-Q. Wu, X.-Y. Gao, W. Zhao, X.-H. Xia, J.-J. Xu and H.-Y. Chen, *Angew. Chem., Int. Ed.*, 2018, **57**, 4074–4078.

56 Y. Ju, H. Zhang, J. Yu, S. Tong, N. Tian, Z. Wang, X. Wang, X. Su, X. Chu, J. Lin, Y. Ding, G. Li, F. Sheng and Y. Hou, *ACS Nano*, 2017, **11**, 9239–9248.

57 F. Zheng, W. Ke, L. Shi, H. Liu and Y. Zhao, *Anal. Chem.*, 2019, **91**, 11812–11820.

58 Y. Su, Q. Zhang, X. Miao, S. Wen, S. Yu, Y. Chu, X. Lu, L.-P. Jiang and J.-J. Zhu, *ACS Appl. Mater. Interfaces*, 2019, **11**, 41979–41987.

59 Y. Feng, Y. Cheng, Y. Chang, H. Jian, R. Zheng, X. Wu, K. Xu, L. Wang, X. Ma, X. Li and H. Zhang, *Biomaterials*, 2019, **217**, 119327.

60 S. Ke, C. Kan, X. Zhu, C. Wang, X. Wang, Y. Chen, X. Zhu, Z. Li and D. Shi, *CrystEngComm*, 2021, **23**, 3467–3476.

61 F. Tao, M. E. Grass, Y. Zhang, D. R. Butcher, J. R. Renzas, Z. Liu, J. Y. Chung, B. S. Mun, M. Salmeron and G. A. Somorjai, *Science*, 2008, **322**, 932.

62 J. Kang, J. Joo, E. J. Kwon, M. Skalak, S. Hussain, Z.-G. She, E. Ruoslahti, S. N. Bhatia and M. J. Sailor, *Adv. Mater.*, 2016, **28**, 7962–7969.

63 X. Zhong, X. Wang, L. Cheng, Y. a. Tang, G. Zhan, F. Gong, R. Zhang, J. Hu, Z. Liu and X. Yang, *Adv. Funct. Mater.*, 2020, **30**, 1907954.

64 Y. Chen, P.-X. Yuan, A.-J. Wang, X. Luo, Y. Xue, L. Zhang and J.-J. Feng, *Biosens. Bioelectron.*, 2019, **126**, 187–192.

65 A.-J. Wang, X.-Y. Zhu, Y. Chen, P.-X. Yuan, X. Luo and J.-J. Feng, *Sens. Actuators, B*, 2019, **288**, 721–727.

66 H. Zhang, Y. Wang, H. Zhong, J. Li and C. Ding, *ACS Appl. Bio Mater.*, 2019, **2**, 5012–5020.

67 M. Xu, Q. Lu, Y. Song, L. Yang, C. Ren, W. Li, P. Liu, Y. Wang, Y. Zhu and N. Li, *Nano Res.*, 2020, **13**, 2118–2129.

68 B. Liu and J. J. N. R. Liu, *Nano Res.*, 2017, **10**, 1125–1148.

69 S.-S. Li, Q.-Y. Guan, G. Meng, X.-F. Chang, J.-W. Wei, P. Wang, B. Kang, J.-J. Xu and H.-Y. Chen, *Sci. Rep.*, 2017, **7**, 2296.

70 S. S. Li, Q. Y. Guan, M. M. Zheng, Y. Q. Wang, D. J. Ye, B. Kang, J. J. Xu and H. Y. Chen, *Chem. Sci.*, 2017, **8**, 7582–7587.

71 X. Cai, S. Ding, Q. Shi, Z. Lyu, D. Liu, W.-j. Dong, M. Du, P. Dutta, Y. Song, D. Du and Y. Lin, *ACS Appl. Bio Mater.*, 2020, **3**, 5922–5929.

72 S.-S. Li, M. Zhang, J.-H. Wang, F. Yang, B. Kang, J.-J. Xu and H.-Y. Chen, *Anal. Chem.*, 2019, **91**, 8398–8405.

73 S.-S. Li, Y.-Y. Tan, Y. Zhang, M. Liu and A. Liu, *Bioelectrochemistry*, 2021, **140**, 107804.

74 J. Chang, A. Zhang, Z. Huang, Y. Chen, Q. Zhang and D. Cui, *Talanta*, 2019, **198**, 45–54.

75 Y. Dong, C. Yao, Y. Zhu, L. Yang, D. Luo and D. Yang, *Chem. Rev.*, 2020, **120**, 9420–9481.

76 X. Zhou, Q. Pu, H. Yu, Y. Peng, J. Li, Y. Yang, H. Chen, Y. Weng and G. Xie, *J. Colloid Interface Sci.*, 2021, **599**, 752–761.

77 P. P. Jia, H. J. Ji, S. K. Liu, R. Zhang, F. He, L. Zhong and P. P. Yang, *J. Mater. Chem. B*, 2021, **9**, 101–111.

78 M. Chen, D. Wu, S. Tu, C. Yang, D. Chen and Y. Xu, *Biosens. Bioelectron.*, 2021, **173**, 112821.

79 X. Qin, Y. Si, D. Wang, Z. Wu, J. Li and Y. Yin, *Anal. Chem.*, 2019, **91**, 4529–4536.

80 J. Huang, J. H. Huang, H. Bao, X. Ning, C. Yu, Z. Chen, J. Chao and Z. Zhang, *ACS Appl. Bio Mater.*, 2020, **3**, 2489–2498.

81 X.-H. Pham, E. Hahm, T. H. Kim, H.-M. Kim, S. H. Lee, S. C. Lee, H. Kang, H.-Y. Lee, D. H. Jeong, H. S. Choi and B.-H. Jun, *Nano Res.*, 2020, **13**, 3338–3346.

82 Z. Wang, Y. Zhang, E. Ju, Z. Liu, F. Cao, Z. Chen, J. Ren and X. Qu, *Nat. Commun.*, 2018, **9**, 3334.

83 R. Wang, J.-J. Feng, Y. Xue, L. Wu and A.-J. Wang, *Sens. Actuators, B*, 2018, **254**, 1174–1181.

84 E. Ko, V.-K. Tran, S. E. Son, W. Hur, H. Choi and G. H. Seong, *Sens. Actuators, B*, 2019, **294**, 166–176.

85 J. Feng, Y. Li, M. Li, F. Li, J. Han, Y. Dong, Z. Chen, P. Wang, H. Liu and Q. Wei, *Biosens. Bioelectron.*, 2017, **91**, 441–448.

86 L. Yue, J. Wang, Z. Dai, Z. Hu, X. Chen, Y. Qi, X. Zheng and D. Yu, *Bioconjugate Chem.*, 2017, **28**, 400–409.

87 G. Darabdhara, B. Sharma, M. R. Das, R. Boukherroub and S. Szunerits, *Sens. Actuators, B*, 2017, **238**, 842–851.

88 Y. Yang, Q. Liu, Y. Liu, J. Cui, H. Liu, P. Wang, Y. Li, L. Chen, Z. Zhao and Y. Dong, *Biosens. Bioelectron.*, 2017, **90**, 31–38.

89 S. C. Barman, M. F. Hossain, H. Yoon and J. Y. Park, *Biosens. Bioelectron.*, 2018, **100**, 16–22.

90 W. Dong, Y. Ren, Z. Bai, Y. Yang and Q. Chen, *Bioelectrochemistry*, 2019, **128**, 274–282.

91 K. Chen, H. Zhao, Z. Wang and M. Lan, *Anal. Chim. Acta*, 2021, **1169**, 338628.

92 Y. Liu, H. Li, S. Gong, Y. Chen, R. Xie, Q. Wu, J. Tao, F. Meng and P. Zhao, *Sens. Actuators, B*, 2019, **290**, 249–257.

93 T. Wang, Q. Bai, Z. Zhu, H. Xiao, F. Jiang, F. Du, W. W. Yu, M. Liu and N. Sui, *Chem. Eng. J.*, 2021, **413**, 127537.

94 Y. Si, L. Li, X. Qin, Y. Bai, J. Li and Y. Yin, *Anal. Chim. Acta*, 2019, **1057**, 1–10.

95 L. Wu, W. Yin, X. Tan, P. Wang, F. Ding, H. Zhang, B. Wang, W. Zhang and H. Han, *Sens. Actuators, B*, 2017, **248**, 367–373.

96 O. Adeniyi, S. Sicwetsha and P. Mashazi, *ACS Appl. Mater. Interfaces*, 2020, **12**, 1973–1987.

97 N. Kostevšek, I. Abramovič, S. Hudoklin, M. E. Kreft, I. Serša, A. Sepe, J. Vidmar, S. Šturm, M. Spreitzer, J. Ščančar, S. Kobe and K. Žužek Rožman, *Nanoscale*, 2018, **10**, 1308–1321.

98 J. Zhao, C. Wu, L. Zhai, X. Shi, X. Li, G. Weng, J. Zhu, J. Li and J.-W. Zhao, *J. Mater. Chem. C*, 2019, **7**, 8432–8441.

99 M. Aghayan, A. Mahmoudi, M. R. Sazegar and F. Adhami, *J. Mater. Chem. B*, 2021, **9**, 3716–3726.

100 Y. Sun, H. Chen, Y. Huang, F. Xu, G. Liu, L. Ma and Z. Wang, *Biomaterials*, 2021, **274**, 120821.

101 L. W. Yap, H. Chen, Y. Gao, K. Petkovic, Y. Liang, K. J. Si, H. Wang, Z. Tang, Y. Zhu and W. Cheng, *Nanoscale*, 2017, **9**, 7822–7829.

102 Q. Yang, P. Wang, E. Ma, H. Yu, K. Zhou, C. Tang, J. Ren, Y. Li, Q. Liu and Y. Dong, *Bioelectrochemistry*, 2021, **138**, 107713.

103 E. Ma, P. Wang, Q. Yang, H. Yu, F. Pei, Y. Zheng, Q. Liu, Y. Dong and Y. Li, *ACS Biomater. Sci. Eng.*, 2020, **6**, 1418–1427.

104 K. Jagajjanani Rao and S. Paria, *J. Cleaner Prod.*, 2017, **165**, 360–368.

105 J.-X. Liu, X.-L. Liang, F. Chen and S.-N. Ding, *Sens. Actuators, B*, 2019, **300**, 127046.

106 Y. Zhang, D. Deng, X. Zhu, S. Liu, Y. Zhu, L. Han and L. Luo, *Anal. Chim. Acta*, 2018, **1042**, 20–28.

107 Y. Li, Y. Zhang, F. Li, J. Feng, M. Li, L. Chen and Y. Dong, *Biosens. Bioelectron.*, 2017, **92**, 33–39.

108 Z. Tan, H. Dong, Q. Liu, H. Liu, P. Zhao, P. Wang, Y. Li, D. Zhang, Z. Zhao and Y. Dong, *Biosens. Bioelectron.*, 2019, **142**, 111556.

109 Y. Li, Y. Wang, L. Bai, H. Lv, W. Huang, S. Liu, S. Ding and M. Zhao, *Anal. Chim. Acta*, 2020, **1125**, 86–93.

110 G. Chen, Y. Qin, L. Jiao, J. Huang, Y. Wu, L. Hu, W. Gu, D. Xu and C. Zhu, *Anal. Chem.*, 2021, **93**, 6881–6888.

111 Z. Jie, G. Qi, C. Xu and Y. Jin, *Anal. Chem.*, 2019, **91**, 14074–14079.

112 J. Zhang, X. Xu and Y. Qiang, *Sens. Actuators, B*, 2020, **312**, 127964.

113 F. Zhang, F. Huang, W. Gong, F. Tian, H. Wu, S. Ding, S. Li and R. Luo, *J. Electroanal. Chem.*, 2021, **882**, 115032.

114 W. Xu, Z. Qin, Y. Hao, Q. He, S. Chen, Z. Zhang, D. Peng, H. Wen, J. Chen, J. Qiu and C. Li, *Biosens. Bioelectron.*, 2018, **113**, 148–156.

115 J. Zeng, M. Gong, D. Wang, M. Li, W. Xu, Z. Li, S. Li, D. Zhang, Z. Yan and Y. Yin, *Nano Lett.*, 2019, **19**, 3011–3018.

116 Z. Sun, S. Fang and Y. H. Hu, *Chem. Rev.*, 2020, **120**, 10336–10453.

117 S. Manzeli, D. Ovchinnikov, D. Pasquier, O. V. Yazyev and A. Kis, *Nat. Rev. Mater.*, 2017, **2**, 17033.

118 A. K. Singh, P. Kumar, D. J. Late, A. Kumar, S. Patel and J. Singh, *Appl. Mater. Today*, 2018, **13**, 242–270.

119 L. Cheng, C. Yuan, S. Shen, X. Yi, H. Gong, K. Yang and Z. Liu, *ACS Nano*, 2015, **9**, 11090–11101.

120 S. Lv, Y. Tang, K. Zhang and D. Tang, *Anal. Chem.*, 2018, **90**, 14121–14125.

121 J. Yang and Y.-W. Yang, *Small*, 2020, **16**, 1906846.

122 Q. Fu, Z. Wu, D. Du, C. Zhu, Y. Lin and Y. Tang, *ACS Sens.*, 2017, **2**, 789–795.

123 S. Bai, D. Serien, A. Hu and K. Sugioka, *Adv. Funct. Mater.*, 2018, **28**, 1706262.

124 J. Wu, K. Qin, D. Yuan, J. Tan, L. Qin, X. Zhang and H. Wei, *ACS Appl. Mater. Interfaces*, 2018, **10**, 12954–12959.

125 G. Panthi and M. Park, *J. Hazard. Mater.*, 2022, **424**, 127565.

126 X. Yang, X. Han, Y. Zhang, J. Liu, J. Tang, D. Zhang, Y. Zhao and Y. Ye, *Anal. Chem.*, 2020, **92**, 12002–12009.

127 L. Liu, K. Ye, C. Lin, Z. Jia, T. Xue, A. Nie, Y. Cheng, J. Xiang, C. Mu, B. Wang, F. Wen, K. Zhai, Z. Zhao, Y. Gong, Z. Liu and Y. Tian, *Nat. Commun.*, 2021, **12**, 3870.

128 S. Li, T. Wei, M. Tang, F. Chai, F. Qu and C. Wang, *Sens. Actuators, B*, 2018, **255**, 1471–1481.

129 S. Balasurya, D. A. Al Farraj, A. M. Thomas, N. A. Alkubaisi, L. L. Raju, A. Das and S. Sudheer Khan, *J. Environ. Chem. Eng.*, 2020, **8**, 104305.

130 H. Zhu, X. Tan, L. Tan, H. Zhang, H. Liu, M. Fang, T. Hayat and X. Wang, *ACS Sustainable Chem. Eng.*, 2018, **6**, 5206–5213.

131 Z. Lu, F. He, C. Y. Hsieh, X. Wu, M. Song, X. Liu, Y. Liu, S. Yuan, H. Dong, S. Han, P. Du and G. Xing, *ACS Appl. Nano Mater.*, 2019, **2**, 1664–1674.

132 Y. J. Yang, W. X. Li and J. W. Liu, *Anal. Chim. Acta*, 2021, **1147**, 124–143.

133 Z.-J. Xie, M.-R. Shi, L.-Y. Wang, C.-F. Peng and X.-L. Wei, *Microchim. Acta*, 2020, **187**, 255.

134 E. W. Miller, A. E. Albers, A. Pralle, E. Y. Isacoff and C. J. Chang, *J. Am. Chem. Soc.*, 2005, **127**, 16652–16659.

135 B. Perillo, M. Di Donato, A. Pezone, E. Di Zazzo, P. Giovannelli, G. Galasso, G. Castoria and A. Migliaccio, *Exp. Mol. Med.*, 2020, **52**, 192–203.

136 T. Konno, E. P. Melo, J. E. Chambers and E. Avezov, *Cells*, 2021, **10**, 233.

137 Y. Ding, B. Yang, H. Liu, Z. Liu, X. Zhang, X. Zheng and Q. Liu, *Sens. Actuators, B*, 2018, **259**, 775–783.

138 L. Jansson and C. Hellerstrom, *Am. J. Physiol.*, 1986, **251**, E644–E647.

139 S. Cai, Z. Fu, W. Xiao, Y. Xiong, C. Wang and R. Yang, *ACS Appl. Mater. Interfaces*, 2020, **12**, 11616–11624.

140 Z. Yang, X. Zheng and J. Zheng, *Chem. Eng. J.*, 2017, **327**, 431–440.

141 J. Li, H. Jin, M. Wei, W. Ren, J. Wang, Y. Zhang, L. Wu and B. He, *Sens. Actuators, B*, 2021, **331**, 129401.

142 K. Tian, Y. Ma, Y. Liu, M. Wang, C. Guo, L. He, Y. Song, Z. Zhang and M. Du, *Sens. Actuators, B*, 2020, **303**, 127199.

143 Q. Zhu, B. Liang, Y. Liang, L. Ji, Y. Cai, K. Wu, T. Tu, H. Ren, B. Huang, J. Wei, L. Fang, X. Liang and X. Ye, *Biosens. Bioelectron.*, 2020, **153**, 112019.

144 J. Chen, G. Cheng, K. Wu, A. Deng and J. Li, *Electrochim. Acta*, 2020, **361**, 137061.

145 X. Zhu, L. Gao, L. Tang, B. Peng, H. Huang, J. Wang, J. Yu, X. Ouyang and J. Tan, *Biosens. Bioelectron.*, 2019, **146**, 111756.

146 T. Chen, J. Xu, M. Arsalan, Q. Sheng, J. Zheng, W. Cao and T. Yue, *Talanta*, 2019, **198**, 78–85.

147 S. Singh, P. Tripathi, N. Kumar and S. Nara, *Biosens. Bioelectron.*, 2017, **92**, 280–286.

148 S.-S. Li, Y.-Y. Hu, A.-J. Wang, X. Weng, J.-R. Chen and J.-J. Feng, *Sens. Actuators, B*, 2015, **208**, 468–474.

149 C. Wang, L. Hu, K. Zhao, A. Deng and J. Li, *Electrochim. Acta*, 2018, **278**, 352–362.

150 S. Yakubu, J. Xiao, J. Gu, J. Cheng, J. Wang, X. Li and Z. Zhang, *Sens. Actuators, B*, 2020, **325**, 128909.

151 L. Wu and X. Qu, *Chem. Soc. Rev.*, 2015, **44**, 2963–2997.

152 M. Labib, E. H. Sargent and S. O. Kelley, *Chem. Rev.*, 2016, **116**, 9001–9090.

153 S. M. Hanash, S. J. Pitteri and V. M. Faca, *Nature*, 2008, **452**, 571–579.

154 A. Iglesias-Mayor, O. Amor-Gutiérrez, A. Novelli, M.-T. Fernández-Sánchez, A. Costa-García and A. de la Escosura-Muñiz, *Anal. Chem.*, 2020, **92**, 7209–7217.

155 S. Zhang, C. Zhang, Y. Jia, X. Zhang, Y. Dong, X. Li, Q. Liu, Y. Li and Z. Zhao, *Bioelectrochemistry*, 2019, **128**, 140–147.

156 L. Yang, M. X. Gao, L. Zhan, M. Gong, S. J. Zhen and C. Z. Huang, *Nanoscale*, 2017, **9**, 2640–2645.

157 X. Weng, Y. Liu, Y. Xue, A.-J. Wang, L. Wu and J.-J. Feng, *Sens. Actuators, B*, 2017, **250**, 61–68.

158 A.-J. Wang, X.-Y. Zhu, Y. Chen, X. Luo, Y. Xue and J.-J. Feng, *Sens. Actuators, B*, 2019, **292**, 164–170.

159 R. Wang, J.-J. Feng, W.-D. Liu, L.-Y. Jiang and A.-J. Wang, *Biosens. Bioelectron.*, 2017, **96**, 152–158.

160 E. Ma, P. Wang, Q. Yang, H. Yu, F. Pei, Y. Li, Q. Liu and Y. Dong, *Biosens. Bioelectron.*, 2019, **142**, 111580.

161 Z. Xi, K. Wei, Q. Wang, M. J. Kim, S. Sun, V. Fung and X. Xia, *J. Am. Chem. Soc.*, 2021, **143**, 2660–2664.

162 R. Wang, W.-D. Liu, A.-J. Wang, Y. Xue, L. Wu and J.-J. Feng, *Biosens. Bioelectron.*, 2018, **99**, 458–463.

163 R. Wang, A.-J. Wang, W.-D. Liu, P.-X. Yuan, Y. Xue, X. Luo and J.-J. Feng, *Biosens. Bioelectron.*, 2018, **102**, 276–281.

164 Y.-C. Shi, A.-J. Wang, P.-X. Yuan, L. Zhang, X. Luo and J.-J. Feng, *Biosens. Bioelectron.*, 2018, **111**, 47–51.

165 Y. Liu, M. Pan, W. Wang, Q. Jiang, F. Wang, D.-W. Pang and X. Liu, *Anal. Chem.*, 2019, **91**, 2086–2092.

166 J. R. Wang, C. Xia, L. Yang, Y. F. Li, C. M. Li and C. Z. Huang, *Anal. Chem.*, 2020, **92**, 4046–4052.

167 Y. Chen, X.-Y. Ge, S.-Y. Cen, A.-J. Wang, X. Luo and J.-J. Feng, *Sens. Actuators, B*, 2020, **311**, 127931.

168 S. K. Gurmessa, L. T. Tufa, J. Kim, K.-I. Lee, Y.-M. Kim, V. T. Tran, H.-Q. Nguyen, T. S. Shim, J. Kim, T. J. Park, J. Lee and H.-J. Kim, *ACS Appl. Nano Mater.*, 2021, **4**, 539–549.

169 S. Palanisamy, D. Senthil Raja, B. Subramani, T.-H. Wu and Y.-M. Wang, *ACS Appl. Mater. Interfaces*, 2020, **12**, 32468–32476.

170 Y. Si, Y. Bai, X. Qin, J. Li, W. Zhong, Z. Xiao, J. Li and Y. Yin, *Anal. Chem.*, 2018, **90**, 3898–3905.

171 G. Qiu, S. P. Ng and C.-M. L. Wu, *Sens. Actuators, B*, 2018, **265**, 459–467.

172 Z. Huang, R. Zhang, H. Chen, W. Weng, Q. Lin, D. Deng, Z. Li and J. Kong, *Biosens. Bioelectron.*, 2019, **142**, 111542.

173 X. Xi, M. Wen, S. Song, J. Zhu, W. Wen, X. Zhang and S. Wang, *Chem. Commun.*, 2020, **56**, 6039–6042.

174 H. Dong, L. Cao, H. Zhao, S. Liu, Q. Liu, P. Wang, Z. Xu, S. Wang, Y. Li, P. Zhao and Y. Li, *Biosens. Bioelectron.*, 2020, **170**, 112667.

175 X.-Y. Wang, Y.-G. Feng, A.-J. Wang, L.-P. Mei, X. Luo, Y. Xue and J.-J. Feng, *Bioelectrochemistry*, 2021, **140**, 107802.

176 Z. Fu, W. Zeng, S. Cai, H. Li, J. Ding, C. Wang, Y. Chen, N. Han and R. Yang, *J. Colloid Interface Sci.*, 2021, **604**, 113–121.

177 D. Liu, C. Ju, C. Han, R. Shi, X. Chen, D. Duan, J. Yan and X. Yan, *Biosens. Bioelectron.*, 2021, **173**, 112817.

178 Y. Lin, S. Xu, J. Yang, Y. Huang, Z. Chen, B. Qiu, Z. Lin, G. Chen and L. Guo, *Sens. Actuators, B*, 2018, **267**, 502–509.

179 J. Das, I. Ivanov, E. H. Sargent and S. O. Kelley, *J. Am. Chem. Soc.*, 2016, **138**, 11009–11016.

180 K. Wolska-Gawron, J. Bartosińska and D. Krasowska, *Arch. Dermatol. Res.*, 2020, **312**, 317–324.

181 M. M. H. Sohel, *Life Sci.*, 2020, **248**, 117473.

182 H. Park, M. K. Masud, J. Na, H. Lim, H.-P. Phan, Y. V. Kaneti, A. A. Alothman, C. Salomon, N.-T. Nguyen, M. S. A. Hossain and Y. Yamauchi, *J. Mater. Chem. B*, 2020, **8**, 9512–9523.

183 S. Mei, B. Liu, X. Xiong and X. Hun, *J. Pharm. Biomed. Anal.*, 2020, **186**, 113280.

184 F. Papaccio, F. Paino, T. Regad, G. Papaccio, V. Desiderio and V. Tirino, *Stem Cells Transl. Med.*, 2017, **6**, 2115–2125.

185 K. Fujita, M. Kamiya and Y. Urano, *Methods Mol. Biol.*, 2021, **2274**, 193–206.

186 G.-W. Wu, Y.-M. Shen, X.-Q. Shi, H.-H. Deng, X.-Q. Zheng, H.-P. Peng, A.-L. Liu, X.-H. Xia and W. Chen, *Anal. Chim. Acta*, 2017, **971**, 88–96.

187 J. Du, Z. Gu, L. Yan, Y. Yong, X. Yi, X. Zhang, J. Liu, R. Wu, C. Ge, C. Chen and Y. Zhao, *Adv. Mater.*, 2017, **29**, 1701268.

188 H. Liu, W. Lin, L. He and T. Chen, *Biomaterials*, 2020, **226**, 119545.

189 X. Ding, P. Yuan, N. Gao, H. Zhu, Y. Y. Yang and Q.-H. Xu, *Nanomed.: Nanotechnol. Biol. Med.*, 2017, **13**, 297–305.

190 B. Hu, F. Kong, X. Gao, L. Jiang, X. Li, W. Gao, K. Xu and B. Tang, *Angew. Chem., Int. Ed.*, 2018, **57**, 5306–5309.

191 P. Yuan, R. Ma, N. Gao, M. Garai and Q.-H. Xu, *Nanoscale*, 2015, 7, 10233–10239.

192 P. Yuan, X. Ding, Z. Guan, N. Gao, R. Ma, X.-F. Jiang, Y. Y. Yang and Q.-H. Xu, *Adv. Healthcare Mater.*, 2015, **4**, 674–678.

193 F. Han, Z. Guan, T. S. Tan and Q.-H. Xu, *ACS Appl. Mater. Interfaces*, 2012, **4**, 4746–4751.

194 K. Aleshire, I. M. Pavlovetc, R. Collette, X. T. Kong, P. D. Rack, S. B. Zhang, D. J. Masiello, J. P. Camden, G. V. Hartland and M. Kuno, *Proc. Natl. Acad. Sci. U.S.A.*, 2020, **117**, 2288–2293.

195 C. Kuppe, X. Z. Zheng, C. Williams, A. W. A. Murphy, J. T. Collins, S. N. Gordeev, G. A. E. Vandenbosch and V. K. Valev, *Nanoscale Horiz.*, 2019, **4**, 1056–1062.

196 S. S. Li, Q. Y. Kong, M. Zhang, F. Yang, B. Kang, J. J. Xu and H. Y. Chen, *Anal. Chem.*, 2018, **90**, 3833–3841.

197 T. Tumkur, X. Yang, C. Zhang, J. Yang, Y. Zhang, G. V. Naik, P. Nordlander and N. J. Halas, *Nano Lett.*, 2018, **18**, 2040–2046.

198 M. M. Richter, *Chem. Rev.*, 2004, **104**, 3003–3036.

199 Y. Fang, H.-M. Wang, Y.-X. Gu, L. Yu, A.-J. Wang, P.-X. Yuan and J.-J. Feng, *Anal. Chem.*, 2020, **92**, 3206–3212.

200 N. Zhang, X.-T. Wang, Z. Xiong, L.-Y. Huang, Y. Jin, A.-J. Wang, P.-X. Yuan, Y.-B. He and J.-J. Feng, *Anal. Chem.*, 2021, **93**, 17110–17118.

201 J. Hu, S. Zhou, Y. Sun, X. Fang and L. Wu, *Chem. Soc. Rev.*, 2012, **41**, 4356–4378.

202 B. Weigelt, J. L. Peterse and L. J. van't Veer, *Nat. Rev. Cancer*, 2005, **5**, 591–602.

203 Y. Yang, J. Huang, X. Yang, K. Quan, H. Wang, L. Ying, N. Xie, M. Ou and K. Wang, *J. Am. Chem. Soc.*, 2015, **137**, 8340–8343.

204 M. Luan, M. Shi, W. Pan, N. Li and B. Tang, *Chem. Commun.*, 2019, **55**, 5817–5820.

205 R. Zhan, X. Li, L. Zang and K. Xu, *Analyst*, 2020, **145**, 1008–1013.

206 Y. Song, Q. Shi, C. Zhu, Y. Luo, Q. Lu, H. Li, R. Ye, D. Du and Y. Lin, *Nanoscale*, 2017, **9**, 15813–15824.

207 Y. Wang, B. Yan and L. Chen, *Chem. Rev.*, 2013, **113**, 1391–1428.

208 W. Ma, P. Fu, M. Sun, L. Xu, H. Kuang and C. Xu, *J. Am. Chem. Soc.*, 2017, **139**, 11752–11759.

209 Z. Zhang, K. Bando, A. Taguchi, K. Mochizuki, K. Sato, H. Yasuda, K. Fujita and S. Kawata, *ACS Appl. Mater. Interfaces*, 2017, **9**, 44027–44037.

210 P. Jiang, Y. Hu and G. Li, *Talanta*, 2019, **200**, 212–217.

211 J. He, J. Dong, Y. Hu, G. Li and Y. Hu, *Nanoscale*, 2019, **11**, 6089–6100.

212 H. Zhu, Y. Wang, C. Chen, M. Ma, J. Zeng, S. Li, Y. Xia and M. Gao, *ACS Nano*, 2017, **11**, 8273–8281.

213 J. Cui, R. Jiang, C. Guo, X. Bai, S. Xu and L. Wang, *J. Am. Chem. Soc.*, 2018, **140**, 5890–5894.

214 S. Cho, W. Park, H. Kim, J. R. Jokisaari, E. W. Roth, S. Lee, R. F. Klie, B. Lee and D.-H. Kim, *ACS Appl. Nano Mater.*, 2018, **1**, 4602–4611.

215 C. Wang, W. Fan, Z. Zhang, Y. Wen, L. Xiong and X. Chen, *Adv. Mater.*, 2019, **31**, 1904329.

216 R. Yang, S. Fu, R. Li, L. Zhang, Z. Xu, Y. Cao, H. Cui, Y. Kang and P. Xue, *Theranostics*, 2021, **11**, 107–116.

217 S. Yu, Y. Zhou, Y. Sun, S. Wu, T. Xu, Y.-C. Chang, S. Bi, L.-P. Jiang and J.-J. Zhu, *Angew. Chem., Int. Ed.*, 2021, **60**, 5948–5958.

218 M. Wang, M. Chang, Q. Chen, D. Wang, C. Li, Z. Hou, J. Lin, D. Jin and B. Xing, *Biomaterials*, 2020, **252**, 120093.

219 S. J. Chen, S. C. Wang and Y. C. Chen, *Int. J. Mol. Sci.*, 2021, **22**, 12836.

220 T. G. Davidson, *Am. J. Health-Syst. Pharm.*, 2001, **58**, S8–S15.

221 K. Antunac, *Acta Clin. Croat.*, 2019, **58**, 46–59.

222 S. Li, W. Sun, Y. Luo, Y. Gao, X. Jiang, C. Yuan, L. Han, K. Cao, Y. Gong and C. Xie, *J. Mater. Chem. B*, 2021, **9**, 4643–4653.

223 R. Oun, Y. E. Moussa and N. J. Wheate, *Dalton Trans.*, 2018, **47**, 6645–6653.

224 X. Yang, L. Li, D. He, L. Hai, J. Tang, H. Li, X. He and K. Wang, *J. Mater. Chem. B*, 2017, **5**, 4648–4659.

225 D. I. Abrams, G. Velasco, C. Twelves, R. K. Ganju and G. Bar-Sela, *J. Natl. Cancer Inst. Monogr.*, 2021, **2021**, 107–113.

226 G. H. Nam, Y. Choi, G. B. Kim, S. Kim, S. A. Kim and I. S. Kim, *Adv. Mater.*, 2020, **32**, 2002440.

227 D. F. Zhi, T. Yang, J. O'Hagan, S. B. Zhang and R. F. Donnelly, *J. Controlled Release*, 2020, **325**, 52–71.

228 H. Lv, D. Xu, L. Sun and B. Liu, *J. Phys. Chem. Lett.*, 2020, **11**, 5777–5784.

229 J. M. Chen, T. J. Fan, Z. J. Xie, Q. Q. Zeng, P. Xue, T. T. Zheng, Y. Chen, X. L. Luo and H. Zhang, *Biomaterials*, 2020, **237**, 119827.

230 M. H. Lan, S. J. Zhao, W. M. Liu, C. S. Lee, W. J. Zhang and P. F. Wang, *Adv. Healthcare Mater.*, 2019, **8**, 1900132.

231 Z. Zhou, J. Song, L. Nie and X. Chen, *Chem. Soc. Rev.*, 2016, **45**, 6597–6626.

232 X. Wang, X. Zhong, Z. Liu and L. Cheng, *Nano Today*, 2020, **35**, 100946.

233 Z. Tang, Y. Liu, M. He and W. Bu, *Angew. Chem., Int. Ed.*, 2019, **58**, 946–956.

234 G. Qi, Y. Zhang, J. Wang, D. Wang, B. Wang, H. Li and Y. Jin, *Anal. Chem.*, 2019, **91**, 12203–12211.

235 S. Bai, N. Yang, X. Wang, F. Gong, Z. Dong, Y. Gong, Z. Liu and L. Cheng, *ACS Nano*, 2020, **14**, 15119–15130.

236 Y. Yang, X. Wang, H. Qian and L. Cheng, *Appl. Mater. Today*, 2021, **25**, 101215.

237 W. Fan, B. Yung, P. Huang and X. Chen, *Chem. Rev.*, 2017, **117**, 13566–13638.

238 P. Huang, X. Qian, Y. Chen, L. Yu, H. Lin, L. Wang, Y. Zhu and J. Shi, *J. Am. Chem. Soc.*, 2017, **139**, 1275–1284.

239 J. Kim, S. Oh, Y. C. Shin, C. Wang, M. S. Kang, J. H. Lee, W. Yun, J. A. Cho, D. Y. Hwang, D. W. Han and J. Lee, *Colloids Surf., B*, 2020, **189**, 110839.

240 E. B. Choi and J. H. Lee, *Arch. Metall. Mater.*, 2017, **62**, 1137–1142.

241 S. Chen, X. C. Qiu, B. W. Zhang, J. B. Xu, F. G. Zhong, B. P. Zhu, Y. Zhang, J. Ou-Yang and X. F. Yang, *J. Alloys Compd.*, 2021, **886**, 161143.

242 M. Pietrzak and P. Ivanova, *Sens. Actuators, B*, 2021, **336**, 129736.

243 Y. Huang, J. Ren and X. Qu, *Chem. Rev.*, 2019, **119**, 4357–4412.

244 X. Mu, J. Wang, Y. Li, F. Xu, W. Long, L. Ouyang, H. Liu, Y. Jing, J. Wang, H. Dai, Q. Liu, Y. Sun, C. Liu and X.-D. Zhang, *ACS Nano*, 2019, **13**, 1870–1884.

245 L. Rizzello and P. P. Pompa, *Chem. Soc. Rev.*, 2014, **43**, 1501–1518.

246 H. Ji, K. Dong, Z. Yan, C. Ding, Z. Chen, J. Ren and X. Qu, *Small*, 2016, **12**, 6200–6206.

247 S. Kumar, R. K. Majhi, A. Singh, M. Mishra, A. Tiwari, S. Chawla, P. Guha, B. Satpati, H. Mohapatra, L. Goswami and C. Goswami, *ACS Appl. Mater. Interfaces*, 2019, **11**, 42998–43017.

248 M. Das, U. Goswami, R. Kandimalla, S. Kalita, S. S. Ghosh and A. Chattopadhyay, *ACS Appl. Bio Mater.*, 2019, **2**, 5434–5445.